

Compatibility of DAMA/LIBRA dark matter detection with other searches

Christopher Savage,^{1,*} Graciela Gelmini,^{2,†} Paolo Gondolo,^{3,‡} and Katherine Freese^{4,§}

¹ *William I. Fine Theoretical Physics Institute, School of Physics and Astronomy, University of Minnesota, Minneapolis, MN 55455, USA*

² *Department of Physics and Astronomy, UCLA, 430 Portola Plaza, Los Angeles, CA 90095, USA*

³ *Department of Physics, University of Utah, 115 S 1400 E #201 Salt Lake City, UT 84112, USA*

⁴ *Michigan Center for Theoretical Physics, Department of Physics, University of Michigan, Ann Arbor, MI 48109, USA*

(Dated: October 24, 2018)

The DAMA/NaI and DAMA/LIBRA annual modulation data, which may be interpreted as a signal for the existence of weakly interacting dark matter (WIMPs) in our galactic halo, are examined in light of null results from other experiments: CDMS, XENON10, CRESST I, CoGeNT, TEXONO, and Super-Kamiokande (SuperK). We use the energy spectrum of the combined DAMA modulation data given in 36 bins, and include the effect of channeling. Several statistical tools are implemented in our study: likelihood ratio with a global fit and with raster scans in the WIMP mass and goodness-of-fit (g.o.f.). These approaches allow us to differentiate between the preferred (global best fit) and allowed (g.o.f.) parameter regions. It is hard to find WIMP masses and couplings consistent with all existing data sets; the surviving regions of parameter space are found here. For spin-independent (SI) interactions, the best fit DAMA regions are ruled out to the 3σ C.L., even with channeling taken into account. However, for WIMP masses of ~ 8 GeV some parameters outside these regions still yield a moderately reasonable fit to the DAMA data and are compatible with all 90% C.L. upper limits from negative searches, when channeling is included. For spin-dependent (SD) interactions with proton-only couplings, a range of masses below 10 GeV is compatible with DAMA and other experiments, with and without channeling, when SuperK indirect detection constraints are included; without the SuperK constraints, masses as high as ~ 20 GeV are compatible. For SD neutron-only couplings we find no parameters compatible with all the experiments. Mixed SD couplings are examined: *e.g.* ~ 8 GeV mass WIMPs with $a_n = \pm a_p$ are found to be consistent with all experiments. In short, there are surviving regions at low mass for both SI and SD interactions; if indirect detection limits are relaxed, some SD proton-only couplings at higher masses also survive.

PACS numbers: 95.35.+d

*cmsavage@physics.umn.edu

†gelmini@physics.ucla.edu

‡paolo@physics.utah.edu

§ktfreese@umich.edu

I. INTRODUCTION

Among the best motivated candidates for dark matter are Weakly Interacting Massive Particles (WIMPs). Direct searches for dark matter WIMPs aim at detecting the scattering of WIMPs off of nuclei in a low-background detector. These experiments measure the energy of the recoiling nucleus, and are sensitive to a signal above a detector-dependent energy threshold [1].

The discovery of an annual modulation by the DAMA/NaI experiment [2], confirmed by the new experiment DAMA/LIBRA [3] of the same collaboration, is the only positive signal seen in any dark matter search. The DAMA collaboration has found an annual modulation in its data compatible with the signal expected from dark matter particles bound to our Galactic Halo [4, 5]. However, other direct detection experiments, *e.g.* CDMS [6, 7], CoGeNT [8, 9], COUPP [10, 11], CRESST [12, 13], KIMS [14], TEXONO [15, 16], and XENON10 [17, 18] have not found any signal from WIMPs. It has been difficult to reconcile a WIMP signal in DAMA with the other negative results [19], for the case of canonical WIMP masses $\sim 100\text{GeV}$ with standard weak interactions motivated by Supersymmetry (SUSY). Yet, for light WIMPs, such compatibility was possible. Papers written prior to the latest DAMA/LIBRA results found regions in cross-section and WIMP mass that reconciled all null results with DAMA’s positive signal, even assuming a standard halo model: WIMPs with spin independent interactions [20, 21] in the mass range 5–9 GeV, and WIMPs with spin dependent interactions [22] in the mass range 5–13 GeV were found to be compatible with all existing data. In addition, Ref. [20, 21] studied not only the case of the standard halo model, but also models with dark matter streams; they found that nonstandard velocity distributions could reconcile all the existing data sets including DAMA. Other dark matter explanations invoke inelastic scattering of WIMPs [23].

Since these studies of a few years ago, DAMA/LIBRA has reported new experimental results. First, of particular interest is the new presentation of the modulation data in 36 separate energy bins, which allows much more detailed investigations of the data. Second, in the past year another possible complication has come to light. The DAMA collaboration has pointed out that “channeling” may affect the interpretation of their data. In general only a fraction (known as the quenching factor) of the recoil energy deposited by a WIMP is transferred to electrons and is converted into useful signal in the DAMA detector (*e.g.* ionization or scintillation); the remainder is converted into phonons and heat and goes undetected. Hence measured energies must be corrected for this behavior to obtain the proper recoil energy, by dividing by this quenching factor. The DAMA detector is composed of NaI, with quenching factors $Q_{Na} = 0.3$ and $Q_I = 0.09$. Yet, recently, the DAMA collaboration pointed out that some fraction of the nuclear recoils travel in straight paths along the crystal in such a way as to lose very little energy to other atoms and to heat, giving nearly all their energy to electrons; *i.e.*, for these cases the measured energy corresponds very nearly to the energy deposited by the WIMP and thus have $Q \approx 1$. As a consequence, the detector is sensitive to lower mass WIMPs than previously thought. The DAMA threshold is 2 keVee (electron equivalent). Using the above quenching factors this was thought to correspond to 7 keV recoil energy for sodium and 22 keV recoil energy for iodine; yet, due to channeling the actual threshold for some of the events can be as low as 2 keV. The new channeling studies revived the possibility of DAMA’s compatibility with other data sets, particularly at low masses.

Light neutralinos as WIMPs with masses as low as 2 GeV [24] or 6 GeV [25, 26] have been

considered, even with the cross sections we find necessary for WIMPs to be compatible with the DAMA signal and all other negative searches (for spin independent interactions) [26]. In any event, in this paper we proceed in a purely phenomenological way in choosing the WIMP mass and cross section, with either spin-independent or spin-dependent cross sections. We do not attempt to provide an elementary particle model to support the values of masses and cross sections. As justification of our approach, let us recall that there is no proven particle theory of dark matter. The candidates we are considering are stable neutral particles which have very small cross sections with nucleons. Regarding their production in accelerators, they would escape from the detectors without interacting. Unless there is a concrete specific model relating our neutral candidate to other charged particles (which can, if fact, be observed) there is no way such particles could be found in accelerators. The usual signature searched for in accelerators, for example at LEP, Tevatron or LHC, is the emission of a charged particle related to the neutral particle in question. For example, searching for “neutralinos” one puts bounds on one of its cousins, a “chargino”, or another relative, a “slepton”. Without a detailed model there are no accelerator bounds on neutral dark matter candidates.

An alternative way to search for WIMP dark matter of relevance to this paper is via indirect detection of WIMP annihilation in the Sun. When WIMPs pass through a large celestial body, such as the Sun or the Earth [27, 28], interactions can lead to gravitational capture if enough energy is lost in the collision to fall below the escape velocity. Captured WIMPs soon fall to the body’s core and eventually annihilate with other WIMPs. These annihilations lead to high-energy neutrinos that can be observed by Earth-based detectors such as Super-Kamiokande [29] (SuperK), which currently provides the tightest indirect detection bounds at light WIMP masses, AMANDA [30, 31], IceCube [32] and ANTARES [33]. The annihilation rate depends on the capture rate of WIMPs, which is in turn determined by the WIMP scattering cross section off nuclei in the celestial body. While the Earth is predominantly composed of spinless nuclei, the Sun is mostly made of hydrogen, which has spin. Thus the spin-dependent cross section of WIMPs off nucleons can be probed by measuring the annihilation signals from WIMP annihilation in the Sun. Other indirect detection methods search for WIMPs that annihilate in the Galactic Halo or near the Galactic Center where they produce neutrinos, positrons, or antiprotons that may be seen in detectors on the Earth [34, 35]. Of course, these rely upon additional physics (WIMP annihilation) beyond what direct detection experiments rely on (WIMP scattering). Thermal WIMPs can only achieve the correct relic density today if their annihilation cross sections are fixed to be the value we use when computing the SuperK limits; yet one can imagine alternatives in which case the SuperK bounds should not be used.

In this paper, we reconsider the issue of compatibility of the new DAMA/NaI and DAMA/LIBRA (hereafter DAMA) results with all other experimental results. We use the 36 bins of modulation data and take into account the channeling effect. We restrict our studies to the standard isothermal model for the dark matter halo. We carefully investigate both spin-independent as well as spin-dependent couplings. Our procedure is the following. Assuming the standard dark halo model, we find the viable region by making sure that we produce the correct amplitudes for the DAMA modulation. We then compare this region with the most stringent current experimental constraints from negative searches. We use three different statistical methods to find the DAMA region: the likelihood method with (i) a global fit and (ii) raster scans in the WIMP mass, and (iii) goodness-of-fit. These methods and the different information derived from them are described in detail.

II. DARK MATTER DETECTION

WIMP direct detection experiments seek to measure the energy deposited when a WIMP interacts with a nucleus in the detector [36]. If a WIMP of mass m scatters elastically from a nucleus of mass M , it will deposit a recoil energy $E = (\mu^2 v^2 / M)(1 - \cos \theta)$, where $\mu \equiv mM / (m + M)$ is the reduced mass, v is the speed of the WIMP relative to the nucleus, and θ is the scattering angle in the center of mass frame. The differential recoil rate per unit detector mass for a WIMP mass m , typically given in units of cpd/kg/keV (where cpd is counts per day), can be written as:

$$\frac{dR}{dE} = \frac{\sigma(q)}{2m\mu^2} \rho \eta(E, t) \quad (1)$$

where $q = \sqrt{2ME}$ is the nucleus recoil momentum, $\sigma(q)$ is the WIMP-nucleus cross-section, ρ is the local WIMP density, and information about the WIMP velocity distribution is encoded into the mean inverse speed $\eta(E, t)$,

$$\eta(E, t) = \int_{u > v_{\min}} \frac{f(\mathbf{u}, t)}{u} d^3u. \quad (2)$$

Here

$$v_{\min} = \sqrt{\frac{ME}{2\mu^2}} \quad (3)$$

represents the minimum WIMP velocity that can result in a recoil energy E and $f(\mathbf{u}, t)$ is the (time-dependent) distribution of WIMP velocities \mathbf{u} relative to the detector.

To determine the number of expected recoils for a given experiment and WIMP mass, we integrate Eqn. (1) over the nucleus recoil energy to find the recoil rate R per unit detector mass:

$$R(t) = \int_{E_1/Q}^{E_2/Q} dE \epsilon(QE) \frac{\rho}{2m\mu^2} \sigma(q) \eta(E, t). \quad (4)$$

$\epsilon(QE)$ is the (energy dependent) efficiency of the experiment, due, *e.g.*, to data cuts designed to reduce backgrounds. Q is the quenching factor relating the observed energy E_{det} (in some cases referred to as the electron-equivalent energy) with the actual recoil energy E_{rec} : $E_{det} = QE_{rec}$ (explained in more detail below). The energy range between E_1 and E_2 is that of *observed* energies for some data bin of the detector (where experiments often bin observed recoils by energy). The quenching factor Q depends on the nuclear target and the characteristics of the detector.

The recoiling nucleus will transfer its energy to either electrons, which may be observed as *e.g.* ionization or scintillation in the detector, or to other nuclei, producing phonons and heat. Experiments that do not measure the phonons/heat can only directly measure the fraction of energy Q that goes into the channel that is observed (such as scintillation); we refer to this as the observed energy. Observed energies for experiments that measure only from the electron channel will be quoted in electron-equivalent energies (keVee). Note some detectors can calibrate their energy scales to $E_{det} = E_{rec}$, in which case the quenching factor can be ignored in the above formulations (such calibrations may directly or indirectly involve a quenching factor).

Real experimental apparatus cannot determine the event energies with perfect precision. If the expected amount of energy in the channel an experiment observes due to a nuclear recoil is E' , the *measured* energy will be distributed about E' . The previous formulas apply only for a perfect energy resolution and must be corrected for this finite resolution. The observed rate over a measured energy range E_1 – E_2 , Eqn. (4), should be replaced with

$$R(t) = \int_0^\infty dE \epsilon(QE) \Phi(QE, E_1, E_2) \frac{\rho}{2m\mu^2} \sigma(q) \eta(E, t). \quad (5)$$

Here, $\Phi(E' = QE, E_1, E_2)$ is a response function corresponding to the fraction of events with an expected observed energy $E' = QE$ (*i.e.* the energy that would be observed with perfect energy resolution) that will actually be measured between E_1 and E_2 ; recall E in the above equation is the recoil energy, of which only a fraction Q is converted into a form that is potentially observable. If the measured energies are normally distributed about E' with a (typically energy dependent) standard deviation $\sigma(E')$,

$$\Phi(E', E_1, E_2) = \frac{1}{2} \left[\operatorname{erf} \left(\frac{E_2 - E'}{\sqrt{2}\sigma(E')} \right) - \operatorname{erf} \left(\frac{E_1 - E'}{\sqrt{2}\sigma(E')} \right) \right]. \quad (6)$$

In the limit $\sigma(E') \rightarrow 0$ (perfect energy resolution), Eqn. (5) reduces to Eqn. (4).

For detectors with multiple elements and/or isotopes, the total rate is given by:

$$R_{tot}(t) = \sum_i f_i R_i(t) \quad (7)$$

where f_i is the mass fraction and R_i is the rate (Eqn. (4)) for element/isotope i .

The expected number of recoils observed by a detector is given by:

$$N_{rec} = M_{det} T R \quad (8)$$

where M_{det} is the detector mass and T is the exposure time.

A. Cross-Section

The $\sigma(q)$ cross-section term in Eqns. (1) & (4) is an effective cross-section for scatters with a momentum exchange q . The momentum exchange dependence appears in form factors that arise from the finite size of the nucleus. The total scattering cross-section generally has contributions from spin-independent (SI) and spin-dependent (SD) couplings, with

$$\sigma = \sigma_{SI} + \sigma_{SD}; \quad (9)$$

these two cross-sections are described below.

Spin-independent (SI). For spin-independent WIMP interactions, we make the usual assumption [1] that the cross section σ scales with the square of the nucleus atomic number A and is given by

$$\sigma = \sigma_0 |F(E)|^2 \quad (10)$$

where σ_0 is the zero-momentum WIMP-nuclear cross-section and $F(E)$ is a nuclear form factor, normalized to $F(0) = 1$. For purely scalar interactions,

$$\sigma_{0,SI} = \frac{4\mu^2}{\pi} [Zf_p + (A - Z)f_n]^2. \quad (11)$$

Here Z is the number of protons, $A - Z$ is the number of neutrons, and f_p and f_n are the WIMP couplings to the proton and nucleon, respectively. In most instances, $f_n \sim f_p$; the WIMP-nucleus cross-section can then be given in terms of the WIMP-proton cross-section as a result of Eqn. (11):

$$\sigma_{0,\text{SI}} = \sigma_{p,\text{SI}} \left(\frac{\mu}{\mu_p} \right)^2 A^2 \quad (12)$$

where the μ_p is the proton-WIMP reduced mass, and A is the atomic mass of the target nucleus. In this model, for a given WIMP mass, $\sigma_{p,\text{SI}}$ is the only free parameter.

For the nuclear form factor we use the conventional Helm form [1, 37],

$$F(E) = 3e^{-q^2 s^2/2} \frac{\sin(qr) - qr \cos(qr)}{(qr)^3}, \quad (13)$$

with $s = 0.9$ fm, r is an effective nuclear radius as described in Ref. [37], and $q = \sqrt{2ME}$.

Spin-dependent (SD). The generic form for the spin-dependent WIMP-nucleus cross-section includes two couplings [38], the WIMP-proton coupling a_p and the WIMP-neutron coupling a_n ,

$$\sigma_{SD}(q) = \frac{32\mu^2 G_F^2}{2J+1} [a_p^2 S_{pp}(q) + a_p a_n S_{pn}(q) + a_n^2 S_{nn}(q)]. \quad (14)$$

Here, the quantities a_p and a_n are actually the axial four-fermion WIMP-nucleon couplings in units of $2\sqrt{2}G_F$ [39, 40, 41]. The nuclear structure functions $S_{pp}(q)$, $S_{nn}(q)$, and $S_{pn}(q)$ are functions of the exchange momentum q and are specific to each nucleus. We take the structure functions for Aluminum from Ref. [42]; for Sodium, Iodine, and Xenon from Ref. [43]; and for Silicon and Germanium from Ref. [44]. These and additional structure functions may be found in the review of Ref. [45].

B. Velocity Distribution

The dark matter halo is likely to have a smooth, well mixed (virialized) component that will lead to detectable recoils in direct detection experiments; the simplest model of this component is the Standard Halo Model (SHM) [5]. In addition to this smooth component, the galaxy contains structure from the galaxy formation process that has not yet virialized. This structure includes, *e.g.*, tidal streams of dwarf galaxies in the process of being absorbed by the Milky Way, such as the Sagittarius dwarf galaxy [46, 47, 48, 49, 50]. Any such structure located about the Solar System will also produce scattering events.

For each of these components, the smooth halo background and any structure, we will use a Maxwellian distribution, characterized by an rms velocity dispersion σ_v , to describe the WIMP speeds, and we will allow for the distribution to be truncated at some escape velocity v_{esc} ,

$$\tilde{f}(\mathbf{v}) = \begin{cases} \frac{1}{N_{\text{esc}}} \left(\frac{3}{2\pi\sigma_v^2} \right)^{3/2} e^{-3\mathbf{v}^2/2\sigma_v^2}, & \text{for } |\mathbf{v}| < v_{\text{esc}} \\ 0, & \text{otherwise.} \end{cases} \quad (15)$$

Here

$$N_{\text{esc}} = \text{erf}(z) - 2z \exp(-z^2)/\pi^{1/2}, \quad (16)$$

with $z \equiv v_{\text{esc}}/\bar{v}_0$, is a normalization factor. The most probable speed,

$$\bar{v}_0 = \sqrt{2/3} \sigma_v, \quad (17)$$

is used to generate unitless parameters such as z . For distributions without an escape velocity ($v_{\text{esc}} \rightarrow \infty$), $N_{\text{esc}} = 1$.

The WIMP component (halo or stream) often exhibits a bulk motion relative to us, so that

$$f(\mathbf{u}) = \tilde{f}(\mathbf{v}_{\text{obs}} + \mathbf{u}), \quad (18)$$

where \mathbf{v}_{obs} is the motion of the observer relative to the rest frame of the WIMP component described by Eqn. (15); this motion will be discussed below. For such a velocity distribution, the mean inverse speed, Eqn. (2), becomes

$$\eta(E, t) = \begin{cases} \frac{1}{\bar{v}_0 y}, & \text{for } z < y, x < |y-z| \\ \frac{1}{2N_{\text{esc}}\bar{v}_0 y} \left[\text{erf}(x+y) - \text{erf}(x-y) - \frac{4}{\sqrt{\pi}} y e^{-z^2} \right], & \text{for } z > y, x < |y-z| \\ \frac{1}{2N_{\text{esc}}\bar{v}_0 y} \left[\text{erf}(z) - \text{erf}(x-y) - \frac{2}{\sqrt{\pi}} (y+z-x) e^{-z^2} \right], & \text{for } |y-z| < x < y+z \\ 0, & \text{for } y+z < x \end{cases} \quad (19)$$

where

$$x \equiv v_{\text{min}}/\bar{v}_0, \quad y \equiv v_{\text{obs}}/\bar{v}_0, \quad \text{and} \quad z \equiv v_{\text{esc}}/\bar{v}_0; \quad (20)$$

recall v_{min} is given by Eqn. (3). Here, we use the common notational convention of representing 3-vectors in bold and the magnitude of a vector in the non-bold equivalent, *e.g.* $v_{\text{obs}} \equiv |\mathbf{v}_{\text{obs}}|$.

Due to the motion of the Earth around the Sun, \mathbf{v}_{obs} is time dependent: $\mathbf{v}_{\text{obs}} = \mathbf{v}_{\text{obs}}(t)$. We write this in terms of the Earth's velocity \mathbf{V}_{\oplus} relative to the Sun as

$$\mathbf{v}_{\text{obs}}(t) = \mathbf{v}_{\odot} + V_{\oplus} [\hat{\mathbf{e}}_1 \cos \omega(t - t_1) + \hat{\mathbf{e}}_2 \sin \omega(t - t_1)], \quad (21)$$

where $\omega = 2\pi/\text{year}$, \mathbf{v}_{\odot} is the Sun's motion relative to the WIMP component's rest frame, $V_{\oplus} = 29.8 \text{ km/s}$ is the Earth's orbital speed, and $\hat{\mathbf{e}}_1$ and $\hat{\mathbf{e}}_2$ are the directions of the Earth's velocity at times t_1 and $t_1 + 0.25$ years, respectively. With this form, we have neglected the ellipticity of the Earth's orbit, although the ellipticity is small and, if accounted for, would give only negligible changes in the results of this paper (see Refs. [37, 51] for more detailed expressions). For clarity, we have used explicit velocity vectors rather than the position vectors $\hat{\mathbf{e}}_1$ and $\hat{\mathbf{e}}_2$ used in Refs. [50, 52] and elsewhere (the position vectors are more easily generalized to an elliptical orbit); the two bases are related by $\hat{\mathbf{e}}_1 = -\hat{\mathbf{e}}_2$ and $\hat{\mathbf{e}}_2 = \hat{\mathbf{e}}_1$.

In Galactic coordinates, where $\hat{\mathbf{x}}$ is the direction to the Galactic Center, $\hat{\mathbf{y}}$ the direction of disk rotation, and $\hat{\mathbf{z}}$ the North Galactic Pole,

$$\hat{\mathbf{e}}_1 = (0.9931, 0.1170, -0.01032), \quad (22)$$

$$\hat{\mathbf{e}}_2 = (-0.0670, 0.4927, -0.8676), \quad (23)$$

where we have taken $\hat{\mathbf{e}}_1$ and $\hat{\mathbf{e}}_2$ to be the direction of the Earth's motion at the Spring equinox (March 21, or t_1) and Summer solstice (June 21), respectively.

In this paper, we will take the halo to be a simple non-rotating isothermal sphere [5], also referred to as the Standard Halo Model (SHM); more complicated halo models will be

examined in a future paper. In this model, typical parameters of the Maxwellian distribution for our location in the Milky Way are $\sigma_{\text{SHM}} = 270$ km/s and $v_{\text{esc}} = 650$ km/s, the latter being the speed necessary to escape the Milky Way (WIMPs with speeds in excess of this would have escaped the galaxy, hence the truncation of the distribution in Eqn. (15)). Unlike the Galactic disk (along with the Sun), the halo has essentially no rotation; the motion of the Sun relative to this stationary halo is

$$\mathbf{v}_{\odot,\text{SHM}} = \mathbf{v}_{\text{LSR}} + \mathbf{v}_{\odot,\text{pec}}, \quad (24)$$

where $\mathbf{v}_{\text{LSR}} = (0, 220, 0)$ km/s is the motion of the Local Standard of Rest and $\mathbf{v}_{\odot,\text{pec}} = (10, 13, 7)$ km/s is the Sun's peculiar velocity. The Earth's speed relative to the halo, $v_{\text{obs}}(t)$, is maximized around June 1. The local dark matter density ρ_0 is taken to be the estimated average density in the local neighborhood, 0.3 GeV/cm³.

C. Annual Modulation

It is well known that the count rate in WIMP detectors will experience an annual modulation as a result of the motion of the Earth around the Sun described above [4, 5]. In some cases, but not all, the count rate (Eqn. (1)) has an approximate time dependence

$$\frac{dR}{dE}(E, t) \approx S_0(E) + S_m(E) \cos \omega(t - t_c), \quad (25)$$

where t_c is the time of year at which $v_{\text{obs}}(t)$ is at its maximum. $S_0(E)$ is the average differential recoil rate over a year and $S_m(E)$ is referred to as the modulation amplitude (which may, in fact, be negative). The above equation is a reasonable approximation for the SHM we are considering in this paper, but is not valid for all halo models, particularly at some recoil energies for dark matter streams; see Ref. [53] for a discussion. For the SHM,

$$S_m(E) = \frac{1}{2} \left[\frac{dR}{dE}(E, \text{June 1}) - \frac{dR}{dE}(E, \text{Dec 1}) \right]. \quad (26)$$

Experiments such as DAMA will often give the average amplitude over some interval,

$$S_m = \frac{1}{E_2 - E_1} \int_{E_1}^{E_2} dE S_m(E). \quad (27)$$

D. Parameter Space

Many of the parameters that factor into the expected recoil rates for a scattering detector are unknown, including the WIMP mass, four WIMP-nucleon couplings (SI and SD couplings to each of protons and neutrons), the local WIMP density, and the WIMP velocity distribution in the halo. In this paper, we shall fix the halo model to the SHM and the local density to 0.3 GeV/cm³. In addition, we shall take $f_p = f_n$ (equal SI couplings) so that there are only three independent scattering couplings; the SI coupling will be given in terms of the SI scattering cross-section off the proton, $\sigma_{p,\text{SI}}$. The parameter space we examine will then consist of the four parameters m , $\sigma_{p,\text{SI}}$, a_p , and a_n .

Experiment	Element	Exposure [kg-day]	Energies [keVee]	Quenching Factor (Q)	Efficiency	Constraint (\dagger)	Ref.
DAMA	NaI	2.99×10^5	2–20	0.3, 0.09 (\ddagger)	1	(various)	[3]
CDMS	Si	6.58	5–55	1 (§)	Eqn. (29)	Poisson	[6]
	Ge	397.8	10–100	1 (§)	Eqn. (28)	Poisson	[7]
CoGeNT	Ge	8.38	0.23–4.1	0.2	Eqn. (30)	BP	[8, 9]
CRESST I	Al ₂ O ₃	1.51	0.6–20	1 (§)	1	BP	[12]
TEXONO	Ge	0.338	0.2–8	0.2	Eqn. (33)	MG	[15, 16]
XENON10	Xe	316.4	6.1–36.5	1 (§)	Eqn. (34)	MG	[17, 18]

TABLE I: Experiments used in this study. Notes to the table: (\dagger) MG is the maximum gap method [55], BP is a Poisson statistics based constraint for binned data as described in the text; (\ddagger) some portion of recoils may undergo channeling with $Q \approx 1$ (see text); (§) energies scaled to recoil energies.

III. NULL EXPERIMENTS

Numerous experiments have searched for a dark matter signal, but all these experimental results, apart from DAMA, are consistent with no WIMP signal. Here, we shall examine the constraints from these null results; the positive DAMA signal will be addressed in the next section. We include here only a few experiments that provide some of the strongest constraints at various points in the WIMP mass-coupling parameter space. We further restrict ourselves to experiments that provide sufficient data for us to independently generate constraints. Notably, this excludes COUPP [10, 11] for which insufficient information on the data runs is provided to both reproduce their results and extend them to arbitrary couplings. COUPP is likely to provide strong constraints in areas of parameter space that other direct detection experiments do not probe and could significantly affect our results. The experiments we include are listed in Table I.

Most of the experiments observe some recoils; these recoils may be due to background events (*e.g.* neutrons from cosmic ray showers), WIMP scatters, or a combination of the two. While tighter constraints may be found by modelling the background contribution, we produce conservative constraints by analyzing the experimental results *without* background subtraction. Additionally, some of the data we use (as presented in the literature) is binned, whereas analysis of the unbinned data (as available to the experimental groups) generally allows for better constraints on the parameter space. Some experiments are also able to combine and analyze their data sets more effectively than we can. Where other ambiguities arise, we err on the side of caution. For these reasons, our constraints are generally more conservative (by as much as a factor of ~ 3 in some cases) than those provided by the experimental groups themselves. Readers should refer to the original experimental publications for more thorough analyses and, in some cases, the inclusion of background subtraction.

We will adopt the standard convention of displaying 90% C.L. exclusion regions for these null experiments. For comparison, however, we will also indicate the parameter space excluded at 3σ and 5σ for a few of the experiments. We will first give a description of the null experiments used in our analysis, then we will describe the various statistical methods used to provide the constraints for these experiments.

A. Descriptions

CDMS. CDMS II has a large exposure for its Germanium detectors, 397.8 kg-days, with a threshold of 10 keV [7]. Observed energies are calibrated to recoil energies, so no quenching factor is required. The efficiency of observing nuclear recoils after data cuts is:

$$\varepsilon(E) = \begin{cases} 0.25 + 0.05 \frac{(E-10 \text{ keV})}{5 \text{ keV}} & \text{for } 10 \text{ keV} < E < 15 \text{ keV}, \\ 0.30 & \text{for } 20 \text{ keV} < E < 100 \text{ keV}. \end{cases} \quad (28)$$

While newer data sets exist, we also include the Silicon data set from CDMS-SUF [6] due to the low 5 keV threshold, which is lower than the 7 & 10 keV thresholds of the newer CDMS II Si data sets. This CDMS-SUF set involves 65.8 kg-days exposure on a 0.100 kg Si detector. With an 80% muon anti-coincident cut efficiency, 95% nuclear recoil band cut efficiency, and additional energy-dependent cuts, the total efficiency can be approximated by¹:

$$\varepsilon(E) = 0.80 \times 0.95 \times \begin{cases} 0.10 + 0.30 \frac{(E-5 \text{ keV})}{15 \text{ keV}} & \text{for } 5 \text{ keV} < E < 20 \text{ keV}, \\ 0.40 + 0.10 \frac{(E-20 \text{ keV})}{80 \text{ keV}} & \text{for } 20 \text{ keV} < E < 100 \text{ keV}. \end{cases} \quad (29)$$

Over a 5–100 keV recoil energy range, two events were detected at 55 & 95 keV that are consistent with expected backgrounds. In our analysis, we will use zero observed events over a 5–55 keV recoil range. While it is not a statistically sound practice to *a posteriori* select the bin to avoid observed events, we are primarily interested in this data set to examine low mass ($\lesssim 30$ GeV) WIMPs, for which the observed events are at energies too high to be compatible with WIMP scatters. As such, using the chosen bin will result in constraints comparable to more formal statistical methods, such as S. Yellin’s maximum gap method [55], at low WIMP masses. For higher mass WIMP constraints based solely on this Silicon data, the two observed events should be included over *e.g.* a 5–100 keV range. With inclusion of the Ge data, however, the contribution of Silicon to the constraints at higher WIMP masses is negligible.

For the combined CDMS Si+Ge data set, we use Poisson statistics to provide a constraint based upon zero observed events.

CoGeNT. This experiment has a low exposure, 8.38 kg-days, on Germanium detectors, but has a very low threshold of 0.23 keVee [8, 9]. Data is binned in observed energies. The CoGeNT collaboration has provided us with data in smaller bins than given in their paper; the lowest energy bins and the number of observed events in those bins are presented in Table II [9]. From the number of events, exposure, and $\frac{dR}{dE}$ values in each bin, we estimate the efficiency to be:

$$\varepsilon(E') = 0.66 - \frac{E'}{50 \text{ keV}}, \quad (30)$$

where the efficiency is given as a function of *observed* energy ($E' = QE$). We take the quenching factor to be $Q_{Ge} = 0.20$. The widths of the bins are smaller than the energy resolution of the CoGeNT detector, so the latter must be taken into account when analyzing their results. The energy resolution used by CoGeNT is:

$$\sigma(E') = \sqrt{(69.7 \text{ eV})^2 + (0.98 \text{ eV})E'}. \quad (31)$$

¹ See also Fig. (3) of Ref. [54], but note that figure imposes a cut-off at 10 keV and an additional 75% cut over 10–20 keV due to problems in one of the Ge detectors; such cuts do not apply in this case.

Energy [keVee]	Events	Energy [keVee]	Events
0.338 - 0.371	4430	0.661 - 0.693	8
0.371 - 0.403	1104	0.693 - 0.725	5
0.403 - 0.435	140	0.725 - 0.757	18
0.435 - 0.467	29	0.757 - 0.790	15
0.467 - 0.499	12	0.790 - 0.822	12
0.499 - 0.532	12	0.822 - 0.854	5
0.532 - 0.564	19	0.854 - 0.886	12
0.564 - 0.596	9	0.886 - 0.919	16
0.596 - 0.628	12	0.919 - 0.951	9
0.628 - 0.661	8	0.951 - 0.983	8

TABLE II: CoGeNT binned data. Only the lowest energy bins are included here; an additional 98 bins over 0.983–4.14 keVee are not shown. Constraints at low WIMP masses mainly come from these lower energy bins.

There are significant background sources that contribute to the large number of observed events. The CoGeNT collaboration assumes specific forms for this background and subtracts it during their analysis. Here, we make no assumptions on the background and perform no background analysis, so our constraint is more conservative.

For the binned CoGeNT data without background subtraction, we generate constraints using the binned Poisson method described below.

CRESST I. CRESST I used Al_2O_3 detectors with an exposure of 1.51 kg-days over an energy of 0.6–20 keV [12]. The energy scale is calibrated to the recoil energy. Only scattering off of Aluminum is considered for the spin-dependent scattering case (Oxygen is ignored). The energy resolution used by CRESST I is:

$$\sigma(E) = \sqrt{(0.220 \text{ keV})^2 + (0.017E)^2} \quad (32)$$

Data is binned with a significant presence of backgrounds. We generate the CRESST I constraints using the binned Poisson method.

TEXONO. Another low exposure, low threshold Germanium experiment similar to CoGeNT, TEXONO has an exposure of 0.338 kg-days over energies of 0.2–0.8 keVee [15, 16]. The quenching factor is taken to be $Q_{Ge} = 0.2$. The combined efficiency after the ACV (98.3%), CRV (91.5%), and PSD cuts (energy dependent, see Figure 3 of Ref. [15]) is estimated to be:

$$\varepsilon(E') = 0.983 \times 0.915 \times \begin{cases} \frac{(E' - 0.1 \text{ keV})}{0.25 \text{ keV}} & \text{for } 0.1 \text{ keV} < E' < 0.35 \text{ keV}, \\ 1 & \text{for } 0.35 \text{ keV} < E'. \end{cases} \quad (33)$$

The constraints are generated using the unbinned maximum gap method [55], which examines the likelihood of observing the gaps in energy between observed events. TEXONO provides two intervals between event energies, 0.198–0.241 keVee and 1.39–1.87 keVee, that are used for the gaps in this method; other gaps in the full 0.198–8 keVee range are ignored (ignoring other intervals can lead to only more conservative constraints in this type of analysis).

Some concerns have been raised regarding the claimed behavior of TEXONO’s detector response at very low energies that calls into question their low energy results [56]. We shall not address these concerns here.

XENON. XENON10 has a large exposure, 316.4 kg-days, on Xenon over 6.1–36.5 keV [17, 18, 57]; energies are calibrated to recoil energies ($Q = 1$). That calibration depends upon a quantity \mathcal{L}_{eff} , described in their papers, that was initially estimated to be 0.19 with large uncertainties. More recent results indicate it might be lower [57] and we use a conservative value of 0.14. Use of this lower value requires all the nuclear recoil energy scales in the XENON10 data to be multiplied by a factor of 0.19/0.14, *e.g.* the 6.1–36.5 keV energy range is determined by multiplying the original range of 4.6–26.9 keV by this factor. We approximate the energy dependent efficiency by:

$$\varepsilon(E) = 0.46\left(1 - \frac{E}{135 \text{ keV}}\right) \quad (34)$$

and use an energy resolution of [58]

$$\sigma(E) = (0.579 \text{ keV})\sqrt{E/\text{keV}} + 0.021E. \quad (35)$$

XENON10 observed 10 events, with an average background of 7 events expected. We use the maximum gap method to generate XENON10 constraints.

Super-Kamionkande. Aside from the direct detection experiments listed above, we shall also show SuperK constraints from WIMP annihilation in the Sun [29]. SuperK determines these constraints by searching for high energy neutrino products of the WIMP annihilation process at the center of the Sun, where the annihilation rate is dependent upon the capture rate of WIMPs and the capture rate depends upon the scattering cross-section for WIMPs off of nuclei in the Sun. Due to the large proportion of Hydrogen, the neutrino flux is particularly dependent upon the scattering cross-section off of the proton (both SI and SD). While there is a weak dependence on WIMP-neutron scattering cross-section through the trace amounts of heavier elements, we consider here only constraints for WIMP-proton scattering and only in the SD case. The SuperK collaboration also provides SI constraints, but only for combined Earth and Solar WIMP annihilations, which we do not include here. Their SI constraints do not affect our results. The SD constraint is given at a 90% C.L. We have not performed our own reanalysis of the SuperK data and simply present the constraints as determined by the SuperK collaboration’s own analysis (see Ref. [71] for a reanalysis).

The SuperK constraints rely on the following assumptions: (1) the WIMP/anti-WIMP abundance is not highly asymmetric, which would suppress the annihilation rate; (2) the annihilation cross-section is sufficiently high so that the capture rate of WIMPs in the Sun (via scattering off of nuclei in the Sun) is in equilibrium with the annihilation rate; and (3) the WIMP does not annihilate predominantly into the light quarks, which do not yield neutrinos in sufficient quantities and energies to be observed. For the Constrained Minimal Supersymmetric Standard Model, these assumptions are mainly satisfied in the parameter space of interest. In general, however, these assumptions need not be satisfied, so the SuperK constraints should be applied with caution.

Constraints comparison. Constraints for these null experiments are shown in Figure 1 for the case of SI scattering. We show here and in later figures regions excluded at the 90% level; for comparison, exclusion regions at 3σ and 5σ are also shown here for a few of the null experiments. The regions above the curves are excluded. The high exposure

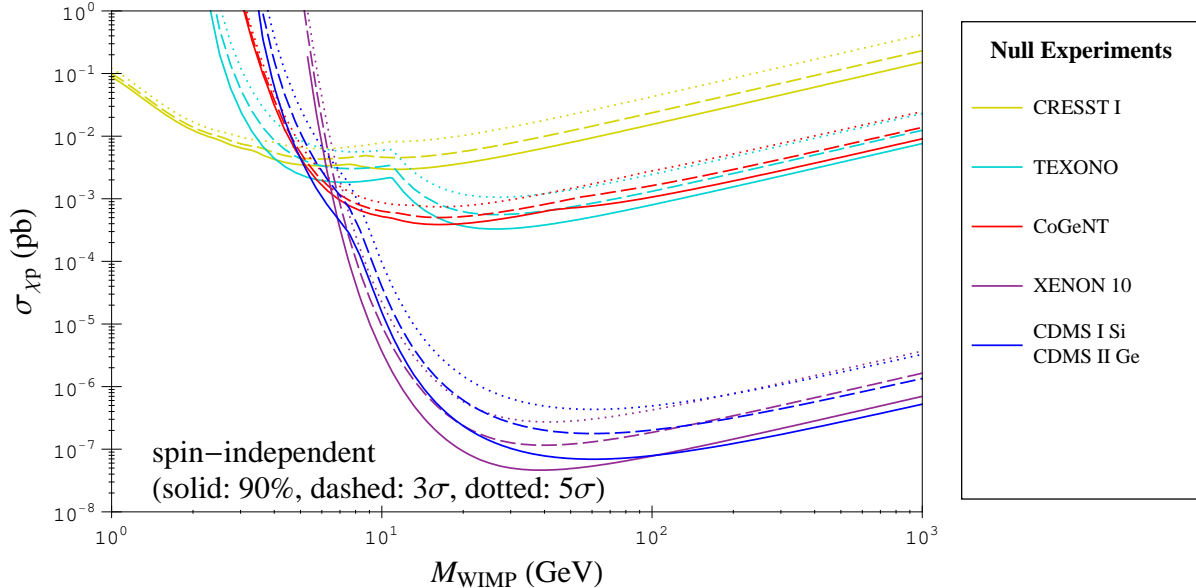


FIG. 1: Constraints on spin-independent (SI) scattering cross-sections for various experiments with null results. Cross-sections below each line are excluded by the given experiment at the 90% (solid), 3σ (dashed), and 5σ (dotted) confidence levels. The same coloring scheme will be used in later figures.

experiments, CDMS and XENON10, provide very strong constraints at high WIMP masses, but provide no constraints at low WIMP masses. Only the low threshold experiments—CoGeNT, CRESST I, and TEXONO—provide constraints at low WIMP masses (due to the fact that light WIMPs only yield low energy collisions, which high threshold experiments cannot detect).

B. Constraints

For the various null experiments, we define constraints in parameter space at a certain exclusion level $1 - \alpha$, typically 90%, as the parameters for which the probability of seeing the experimental result is α . Parameters outside the corresponding contours would yield the observed result with a probability less than α . We say the parameters within those contours are compatible within the $1 - \alpha$ level and parameters outside are excluded at the $1 - \alpha$ level. The probabilities are determined use different statistical values, described here, in different cases.

Poisson. For data in a single bin, we use Poisson statistics to exclude parameter space as follows: parameters that predict an average number of events μ in that bin are excluded at a level of $1 - \alpha$ if the probability of seeing as few as the observed number of events (zero in the case of CDMS Si+Ge) is less than α . For zero observed events, that corresponds to upper limits on μ of 2.3 at a 90% exclusion level, 5.9 at 3σ , and 14.4 at 5σ . Here, we use $N\sigma$ to indicate the probabilities associated with the $\pm N\sigma$ bounds of a normal distribution.

Binned Poisson (BP). For binned data with unknown background, we exclude parameter space using what we shall refer to as a “binned Poisson” (BP) technique, defined as follows.

If α_{bin} is the probability of seeing below a certain number of events in a bin (the lower tail of the Poisson distribution), the probability α of seeing at least one bin measurement falling below the α_{bin} lower tail of that bin is related by:

$$1 - \alpha = (1 - \alpha_{\text{bin}})^{N_{\text{bin}}}, \quad (36)$$

where N_{bin} is the number of bins. For a desired exclusion level of $1 - \alpha$, we then require at least one bin to be at the bin's exclusion level of $1 - \alpha_{\text{bin}}$, where α_{bin} can be determined from α using the above equation. For example, for a desired exclusion level of 90% in two bins, the observed number of events in at least one bin should be excluded at the 94.9% level. In other words, if there is only a 5.1% chance of seeing below a certain number of events in each bin, there is a 10% chance of the observed number of events in at least one those bins to be below that number of events. In practice, the $1 - \alpha$ exclusion contour is determined by, at each WIMP mass, increasing the scattering cross-section until the number of events N_k observed in at least one bin is in the $1 - \alpha_{\text{bin}}$ lower tail of the Poisson distribution with average μ_k , where μ_k is the theoretical predicted average number of events in that bin. Background events make the observed number of events (signal + background) less likely to fall into the lower tail of a Poisson distribution based upon the expected signal alone; bins with larger signal-to-noise will likely be the first to reach the $1 - \alpha_{\text{bin}}$ exclusion level (*i.e.* too few events) and define the overall constraint. Then this technique determines the overall constraint from the bin that would provide the strongest constraint, but takes the required statistical penalty for choosing that bin, since that bin can simply be one in which a statistical fluctuation produces a lower than expected number of events. See Ref. [59] for further discussions. This type of analysis is not optimal, but is simple and straightforward to perform and works reasonably well for the large background cases of CoGeNT and CRESST I here.

Maximum Gap (MG). For unbinned data with unknown background, constraints are generated using S. Yellin's maximum gap (MG) method [55], which examines the likelihood of observing the gaps in energy between observed events. This unbinned method generally provides a stronger constraint than the previous (binned) methods for the case of an unknown background.

IV. DAMA

The DAMA/NaI experiment [2] used a large NaI detector to search for the small modulation in the WIMP scattering rate and became the first direct detection experiment to observe a positive signal. That signal has since been confirmed by the successor to DAMA/NaI, DAMA/LIBRA [3] (also a NaI detector). These two experiments remain the only direct detection experiments to observe a signal.

The original DAMA/NaI experiment released data for only two independent bins, a low energy bin at 2–4, 2–5, or 2–6 keVee (these are not independent) with a non-trivial modulation amplitude and a high energy bin at 6–14 keVee with an amplitude consistent with zero. The DAMA/LIBRA results, in combination with the earlier DAMA/NaI results, have been released for 36 bins over a range of 2–20 keVee (we shall henceforth use “DAMA” to refer to this combined data set). The modulation amplitudes for these bins, taken from Figure 9 of Ref. [3], are given in Table III. The 1σ bounds on the amplitudes for these bins are shown as pink boxes in Figure 2. For comparison, modulation amplitudes are

Energy [keVee]	Average S_m [cpd/kg/keV]	Energy [keVee]	Average S_m [cpd/kg/keV]
2.0 - 2.5	0.0162 ± 0.0048	11.0 - 11.5	-0.0021 ± 0.0039
2.5 - 3.0	0.0287 ± 0.0054	11.5 - 12.0	-0.0010 ± 0.0040
3.0 - 3.5	0.0250 ± 0.0055	12.0 - 12.5	0.0015 ± 0.0040
3.5 - 4.0	0.0140 ± 0.0050	12.5 - 13.0	0.0020 ± 0.0040
4.0 - 4.5	0.0101 ± 0.0045	13.0 - 13.5	-0.0019 ± 0.0040
4.5 - 5.0	0.0118 ± 0.0041	13.5 - 14.0	0.0015 ± 0.0040
5.0 - 5.5	0.0039 ± 0.0041	14.0 - 14.5	-0.0022 ± 0.0040
5.5 - 6.0	0.0030 ± 0.0039	14.5 - 15.0	-0.0008 ± 0.0040
6.0 - 6.5	0.0059 ± 0.0038	15.0 - 15.5	-0.0021 ± 0.0039
6.5 - 7.0	0.0011 ± 0.0036	15.5 - 16.0	-0.0022 ± 0.0038
7.0 - 7.5	-0.0001 ± 0.0036	16.0 - 16.5	0.0053 ± 0.0037
7.5 - 8.0	0.0004 ± 0.0036	16.5 - 17.0	0.0060 ± 0.0037
8.0 - 8.5	-0.0014 ± 0.0037	17.0 - 17.5	0.0007 ± 0.0037
8.5 - 9.0	0.0039 ± 0.0037	17.5 - 18.0	0.0041 ± 0.0035
9.0 - 9.5	-0.0034 ± 0.0037	18.0 - 18.5	0.0011 ± 0.0035
9.5 - 10.0	-0.0071 ± 0.0038	18.5 - 19.0	-0.0014 ± 0.0035
10.0 - 10.5	0.0086 ± 0.0038	19.0 - 19.5	0.0006 ± 0.0034
10.5 - 11.0	-0.0018 ± 0.0039	19.5 - 20.0	0.0056 ± 0.0034
		(†) 10.0 - 20.0	0.0011 ± 0.0008

TABLE III: DAMA/NaI + DAMA/LIBRA (DAMA) modulation amplitudes for the given observed energy bins. Data is taken from Figure 9 of Ref. [3]. (†) The bins over 10-20 keV have been combined into a single bin for use with some of the analysis techniques discussed in the text.

shown in blue boxes for a 2 bin data set: 0.0215 ± 0.0026 cpd/kg/keVee over 2–4 keVee and 0.0005 ± 0.0010 over 6–14 keVee.

We use the quenching factors $Q_{Na} = 0.3$ and $Q_I = 0.09$ in our calculations, with some exceptions as discussed in the following section.

A. Detector Effects

Several physical and instrumental effects add complications to the basic description of experimental recoil rates as described in Section II. These include a finite detector energy resolution and two effects, ion channeling and the Migdal effect, that affect how much of the deposited energy goes into the observed channels.

1. Energy Resolution

The DAMA/LIBRA apparatus, as with all experiments, cannot determine the event energies with perfect precision. If the expected amount of energy in the channel DAMA/LIBRA observes is $E' = QE$, the *measured* energy will be normally distributed about this energy

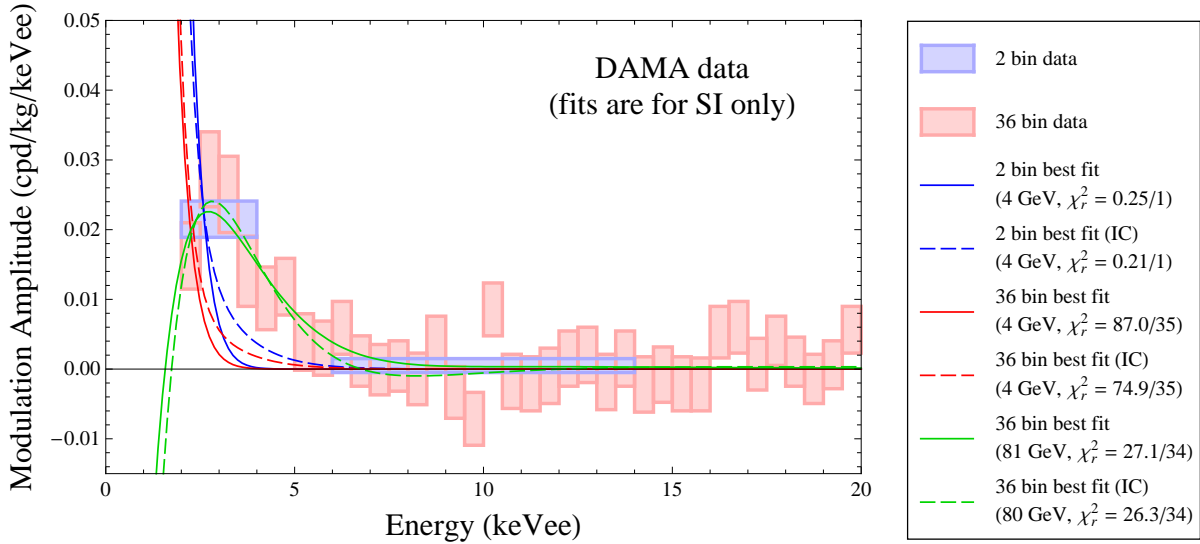


FIG. 2: DAMA modulation amplitude data as well as best fit spectra for various cases. Boxes represent the 1σ bounds of the measured modulation amplitude for each bin: pink for the full 36 bin data set and blue for a 2 bin data set (2–4 & 6–14 keVee). Also shown are the S_m spectra for the best fit SI cross-sections (in the SI only coupling case) at a WIMP mass of 4 GeV for the 2 bin data (blue) and 36 bin data (red), with (dashed) and without (solid) inclusion of the ion channeling (IC) effect. The χ^2 values (over the degrees of freedom) are indicated in the legend. For comparison, the best (SI only) fit at any mass, which occurs around 80 GeV, is shown (green).

with a standard deviation [60],

$$\sigma(E') = (0.448 \text{ keV})\sqrt{E'/\text{keV}} + 0.0091E'. \quad (37)$$

While this equation technically applies only to the DAMA/LIBRA apparatus, we use the same energy resolution for the combined data of DAMA/NaI and DAMA/LIBRA. We include this finite energy resolution in all our DAMA calculations.

2. Ion Channeling

Typically, only a small fraction Q of the recoil energy, 0.3 for Na and 0.09 for I, goes into a mode that DAMA measures (scintillation). The rest is converted into, *e.g.*, phonons/heat as the recoiling nucleus collides with other nuclei and is not observed. As pointed out by the DAMA Collaboration [61], nuclei that recoil along the characteristic axes or planes of the crystal structure may travel large distances without colliding with other nuclei. For ions such as recoiling Na^+ or I^- , the recoil energy in this case is primarily transferred to electrons (which is observable) rather than other nuclei (which becomes heat). Some recoils that undergo this ion channeling (IC) have $Q \approx 1$.

DAMA has used simulations to determine the energy-dependent fractions of recoils off of Na (f_{Na}) and I (f_{I}) that will have $Q \approx 1$ due to this IC effect. These fractions, given by

Figure 4 of Ref. [61], are well approximated by

$$f_{Na} = 10^{-\sqrt{E/(6.9 \text{ keV})}} \quad (38)$$

and

$$f_I = 10^{-\sqrt{E/(11.5 \text{ keV})}}, \quad (39)$$

where these fractions are given as functions of the *recoil* energy.

We shall examine the DAMA results both with and without including the IC effect and shall use “IC” in the figures to indicate those analyses that include it. We have not included this effect in other experiments where it may also be applicable, such as CoGeNT and TEXONO ².

3. Migdal Effect

In the 1940’s, Migdal pointed out that the rapid change in velocity of a recoiling nucleus can cause bound electrons to become excited or ionized [62]. In the DAMA detector, the energy of these ionized electrons goes into observable modes. At the same time, the *apparent* recoil energy is reduced as the energy is lost to the ionized electron almost immediately, before the nucleus travels far enough to interact with other nuclei and electrons. This Migdal effect (ME) can then affect the amount of observed energy coming from a scattering event at a given energy. Due to the complicated nature of this effect, we shall not show its implementation here, but it results in a rather complicated response function Φ that may be used in Eqn. (5). The implementation of the Migdal effect in an analysis of DAMA is fully described in Ref. [63]. We do not include the Migdal effect in our analysis at this time, but we plan to include it in a future paper.

B. Analysis Techniques

There are many possibilities for analyzing the DAMA results; the choice of statistical tests depends upon how one wishes to interpret the results. Here, we will use three different tests to produce different regions in parameter space: a likelihood ratio method with a global fit of four parameters (which we refer to as the “likelihood ratio” method from now on) to find the preferred (best fit) parameters to produce the DAMA signal, a likelihood ratio method with a one parameter fit in raster scans to find the preferred scattering cross-section to produce the DAMA signal at each WIMP mass (which we call the “raster scan”), and a χ^2 goodness-of-fit test (g.o.f.) to indicate which parameters are compatible with the DAMA signal. See Ref. [64] for a short review of statistics or Ref. [65] for more extensive discussions.

² Channeled events in experiments that measure phonons/heat, such as CDMS, would not be seen as any events with relatively high ionization/scintillation and low heat are characteristic of electromagnetic backgrounds (*e.g.* γ -rays), which induce electron rather than nuclear recoils, and are thrown out.

	Mass [GeV]	$\sigma_{p,SI}$ [pb]	a_p ($\sigma_{p,SD}$ [pb])	a_n ($\sigma_{n,SD}$ [pb])	χ^2_{\min} (d.o.f.)
Global	81.0	2.0×10^{-5}	0.0 (0.0)	0.0 (0.0)	27.1 (32)
w/ channeling	78.6	2.7×10^{-5}	0.62 (0.13)	0.70 (0.17)	25.4 (32)
SI only	81.0	2.0×10^{-5}	0 (0)	0 (0)	27.1 (34)
w/ channeling	80.0	3.0×10^{-5}	0 (0)	0 (0)	26.3 (34)
SD only	9.1	0	14.2 (59.4)	-176 (9020)	29.3 (33)
w/ channeling	12.0	0	1.07 (0.35)	-12.8 (50.2)	30.9 (33)
SD proton only	11.5	0	1.70 (0.88)	0 (0)	30.8 (34)
w/ channeling	11.4	0	1.33 (0.53)	0 (0)	31.0 (34)
SD neutron only	11.0	0	0 (0)	20.3 (125)	31.0 (34)
w/ channeling	11.9	0	0 (0)	7.8 (18.6)	30.9 (34)
SD only ($a_n = a_p$)	11.5	0	1.57 (0.75)	1.57 (0.75)	30.8 (34)
w/ channeling	11.4	0	1.15 (0.40)	1.15 (0.40)	31.0 (34)
SD only ($a_n = -a_p$)	11.6	0	1.88 (1.05)	-1.88 (1.05)	30.8 (34)
w/ channeling	11.2	0	1.56 (0.73)	-1.56 (0.73)	31.1 (34)

TABLE IV: Parameters at which the DAMA χ^2 is minimized. The global minimum is found by allowing all parameters (m , $\sigma_{p,SI}$, a_p , and a_n) to vary, while the other cases allow only a subset of these parameters to vary freely with the other parameters fixed to zero or fixed in terms of the free parameters. Bold parameters in the table are those that have been fixed.

1. Likelihood Ratio

To determine the most likely parameters for producing the DAMA signal, we use the maximum likelihood method, based on the likelihood ratio

$$\frac{L(S_{m,k}|m, \sigma_{p,SI}, a_p, a_n)}{L(S_{m,k}|\hat{m}, \hat{\sigma}_{p,SI}, \hat{a}_p, \hat{a}_n)}, \quad (40)$$

where L is the likelihood function, $S_{m,k}$ are the observed modulation amplitudes in each bin, and \hat{m} , $\hat{\sigma}_{p,SI}$, \hat{a}_p , and \hat{a}_n are the values of the parameters that maximize the likelihood for the observed $S_{m,k}$. The denominator of the above equation is the maximum likelihood value L_{\max} . Confidence regions in the parameters are determined by

$$2 \ln L(m, \sigma_{p,SI}, a_p, a_n) \geq 2 \ln L_{\max} - 2 \Delta \ln L, \quad (41)$$

where the value of $\Delta \ln L$ corresponds to the confidence level (C.L.) of the confidence region. Since each bin is normally distributed, this equation may instead be given in terms of the χ^2 ,

$$\chi^2(m, \sigma_{p,SI}, a_p, a_n) \leq \chi^2_{\min} + \Delta \chi^2, \quad (42)$$

where

$$\chi^2(m, \sigma_{p,SI}, a_p, a_n) \equiv \sum_k \frac{(S_{m,k} - S_{m,k}^{\text{Th}})^2}{\sigma_k^2}, \quad (43)$$

σ_k is the uncertainty in $S_{m,k}$ (see Table III), $S_{m,k}^{\text{Th}} \equiv S_{m,k}^{\text{Th}}(m, \sigma_{p,SI}, a_p, a_n)$ is the expected amplitude in a particular bin for the given parameters, and χ^2_{\min} is the minimum value of

χ^2 . The χ_{\min}^2 and the parameters at which it occurs is given in Table IV in this global (four parameter) case both with and without IC. Also given are the minima in various specific cases, such as SI only scattering.

The $\Delta\chi^2$ limit corresponding to different C.L.'s depends upon the number of parameters that have been minimized and, in the large data sample limit, is determined from a χ^2 distribution with the degrees of freedom (d.o.f.) equal to the number of minimized parameters. For the four parameters considered here, $\Delta\chi^2 = 7.8$ (90% C.L.), 16.3 (3σ), 34.6 (5σ), and 60.3 (7σ).

The confidence region for DAMA as described here is, in fact, a 4-dimensional region in the $(m, \sigma_{p,\text{SI}}, a_p, a_n)$ parameter space. We shall be showing 2-dimensional slices of this larger region for particular cases, such as the $a_p = a_n = 0$ slice corresponding to SI only scattering. This is *not* equivalent to fixing $a_p = a_n = 0$ and determining a 2-dimensional confidence region by minimizing only over $(m, \sigma_{p,\text{SI}})$. In the latter case, a confidence region will always be defined in a 2-dimensional plane while, in the former, there may be no slice in that plane if that plane represents a poor “fit” relative to the overall parameter space.

Note, as will be discussed in Section V, the confidence regions obtained via this method yield the most *preferred* (best fit) parameters for producing the signal. This method, in and of itself, does *not* imply parameters outside the confidence regions are necessarily a bad fit to the data (or, conversely, that parameters inside these regions are a good fit) and one should be careful using these regions to compare with other experiments ³.

2. Raster Scan

Since previous papers have examined the possibility of low mass WIMPs as the source of the DAMA signal [20, 21, 22], we include an analysis that gives the preferred scattering cross-sections at a given WIMP mass. If one specified how to determine the preferred cross-sections for an arbitrary WIMP mass, the band formed by these preferred cross-sections over all masses is what is referred to as a raster scan.

The raster scans here involve only two parameters, m and σ , where the WIMP mass m is the parameter we scan over and σ is some scattering cross-section, *e.g.* the SI cross-section (we shall be examining several different cases). At a given m , the preferred values for σ are determined using the likelihood ratio method just described but leaving one parameter, which we call here σ , as a variable and fixing the other two couplings/cross-sections to some value, usually zero. Thus the χ^2 is minimized over σ at that particular mass, $\chi_{\text{RS},\min}^2(m) = \chi^2(m, \hat{\sigma})$. The confidence *interval* in σ at m is then

$$\chi^2(m, \sigma) \leq \chi_{\text{RS},\min}^2(m) + \Delta\chi_{\text{RS}}^2, \quad (44)$$

where limits on $\Delta\chi_{\text{RS}}^2$, determined from a χ^2 distribution with 1 d.o.f. (large data sample limit), are 2.7, 9, 16, and 25 at C.L.'s of 90%, 3σ , 5σ , and 7σ , respectively. The band of confidence *intervals* in σ over all masses defines a confidence *region* in m and σ at the same C.L. as the intervals; we call this region the raster scan region.

The above formulation is not technically correct when physical boundaries are present, such as the requirement of a non-negative cross-section, but it is approximately correct if

³ In statistical parlance, the determination of the confidence region for this method is *decoupled* from the goodness-of-fit.

the obtained confidence intervals are not near the boundary. As will be seen later, the raster scans do yield confidence intervals that cross the physical $\sigma = 0$ boundary; however, these occur only at high WIMP masses that will not be of interest. The raster scans over the masses of interest are far enough from the boundary to be approximately correct. Formally, one should use a method that can appropriately account for such boundary conditions, such as that of Feldman and Cousins [66]⁴.

The raster scan itself, by definition, provides no constraint on the WIMP mass and the raster scan band includes WIMP masses at which no scattering cross-section is capable of reasonably producing the DAMA signal. One may determine which WIMP masses provide poor fits to the DAMA data by applying a χ^2 goodness-of-fit test at the best fit cross-section $\hat{\sigma}$ at the mass to be examined. The χ^2 values at these minima should follow a χ^2 distribution with 35 d.o.f. (36 bins with a fit to 1 parameter (σ)). The χ^2 for 35 d.o.f. is expected to fall below 46.1, 62.8, and 91.7 with probabilities of 90%, 99.73% (3σ), and 99.999943% (5σ), respectively; then the χ^2 should exceed those values only 10%, 0.27% and $5.7 \times 10^{-5}\%$ of the time, respectively.

3. Goodness-of-Fit

To conservatively indicate parameters that are compatible with the DAMA data set, we also indicate regions at which the χ^2 falls within a given level using a simple χ^2 goodness-of-fit (g.o.f.) test on the data. In contrast to the previous two analyses methods, there is no fit to the parameters here. The g.o.f. regions are defined as those parameters for which

$$\chi^2(m, \sigma_{p,SI}, a_p, a_n) \leq \chi_{\text{GOF}}^2, \quad (45)$$

where χ_{GOF}^2 is the value at which the χ^2 cumulative distribution function (CDF) for *e.g.* 36 d.o.f. is equal to the desired level of compatibility. That is, for a desired compatibility level of $1 - \alpha$, there is a probability α that χ^2 will exceed χ_{GOF}^2 . Alternatively, we can say parameters outside of the region are excluded at the $1 - \alpha$ level.

For the SHM, the expected DAMA modulation amplitudes for energies over 10 keVee are negligibly small (statistically equal to zero) over the parameter space examined in this paper. The DAMA modulation amplitude data is then expected to randomly vary about zero in the higher energy bins, which increases the χ^2 and dilutes the power of the g.o.f. test. To improve the ability of the g.o.f. test to exclude some parameters, we combine all DAMA bins over 10-20 keVee into a single bin (0.0011 ± 0.0008 cpd/kg/keVee), resulting in a total of 17 data bins used for this test. The previous two analyses (likelihood ratio and raster scan) are not affected by the numerous high energy bins varying about zero and use the full 36 bin data set. For the 17 d.o.f. χ^2 distribution, values of 24.8, 37.7, and 61.6 are excluded at the 90%, 3σ , and 5σ levels, respectively.

While the g.o.f. regions defined here are, in fact, confidence regions—indicating the likely parameters to produce the DAMA signal in our theoretical framework—we do not use these regions in that manner. The determination of a confidence region *assumes* that the theoretical framework is correct, *i.e.* there exists some choice of parameters that is correct. That

⁴ The result of using this more formal method will be to shift upwards the upper bounds on σ at masses where the confidence interval is near the $\sigma = 0$ boundary, but the shift will be less than a factor of 2.

assumption may not be valid if, *e.g.*, the standard halo model is not a reasonable approximation of the actual halo. Instead, we will more conservatively only use this g.o.f. test to *exclude* parameters outside of the corresponding regions. That is, parameters outside of the DAMA g.o.f. regions are incompatible with the DAMA signal at the given level.

C. Total Rate

While we mainly examine the DAMA experiment by analyzing the modulation amplitude S_m , DAMA can additionally constrain parameter space using the total rate (S_0 in Eqn. (25)) as shown in Figure 1 of Ref. [3]. The DAMA detectors do not strongly discriminate between WIMP scatters and background events, so an unknown and possibly large portion of the total observed events may be due to backgrounds (the backgrounds are presumed not to vary with time and do not contribute to the modulation). In the same manner as the various null experiments, we use the total number of events observed by DAMA in 0.25 keVee width bins over 2-10 keVee to constrain the parameter space by excluding regions that would predict more events than observed. While DAMA shows data for several bins below 2 keVee, we conservatively use only the data above their 2 keVee threshold as the behavior of their detector at low energies may not be well understood. Due to the large number of observed events (in excess of 10,000 in each bin), statistical fluctuations are relatively small and any choice of parameters that predicts an S_0 value exceeding the measured rate by more than a few percent is incompatible with the data to a very high level.

As with the null experiments, we will show regions excluded at the 90% level due to the total rate for DAMA. Constraints will be shown with and without the channeling effect. Note that some choices of parameters that produce the correct modulation signal may actually predict a total rate larger than observed and, hence, those parameter choices are incompatible with the full DAMA data set.

V. RESULTS

Here, we apply the statistical techniques described in the previous section to the DAMA data and make comparisons with the null experiments. We begin by examining how the increase in DAMA data bins affects the results, then we examine the various DAMA detector effects, and finally we compare the various experiments.

A. DAMA Binning

The DAMA/NaI data was only presented for two independent bins, so our earlier analyses (performed prior to DAMA/LIBRA) used only one or two bins. To demonstrate how the increase in the number of DAMA data bins from 2 to 36 has considerably increased the ability to constrain parameter space, we first examine a 2 bin data set. Here, we use the 2 bins from the combined DAMA/NaI + DAMA/LIBRA data set as given in the previous section (2–4 & 6–14 keVee); this may be directly compared with the 36 bin DAMA results, which are derived from the same raw data set. The bins and the 1σ bounds on the amplitudes are shown as blue boxes in Figure 2. The low energy (2–4 keVee) bin has a positive amplitude, while the high energy (6–14 keVee) bin is consistent with no modulation.

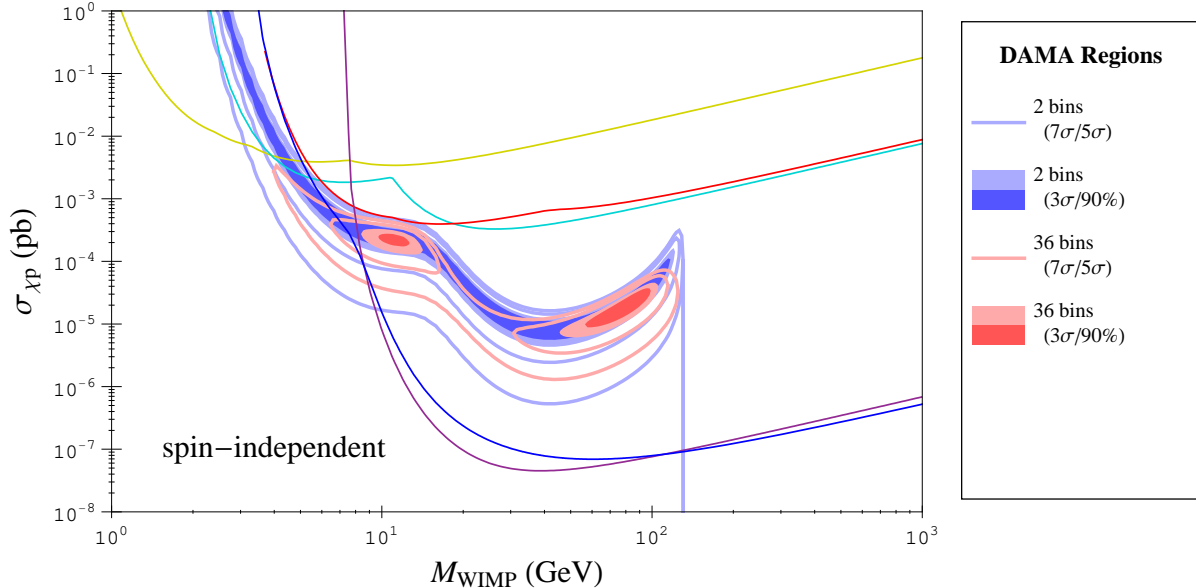


FIG. 3: Most likely parameters to produce the DAMA signal as determined using 2 bins (2–4 & 6–14 keVee; blue) and 36 bins (pink) for the case of SI scattering. The dark/light solid regions correspond to 90%/3 σ confidence regions; these regions are surrounded by 5 σ and 7 σ contours. The 2 bin data set provides very little constraint on the WIMP mass, while the 36 bin constrains the WIMP mass to two regions around 12 GeV and 80 GeV, corresponding to predominantly scattering off of Na and I, respectively. Null experiment constraints as described in Figure 1 are shown at 90% exclusion levels.

In the SHM, there are very few recoils in NaI above 6 keVee, so the expected modulation amplitude in the high energy bin will nearly always be small. In that case, the upper bin provides essentially no constraint on parameter space and there is effectively only one bin (the low energy bin) that yields constraints. Since the amplitude is proportional to the scattering cross-section, as long as a positive modulation is predicted for the low energy bin at some WIMP mass, one can always find a cross-section that yields an excellent fit to the data. Only at very low WIMP masses, where the recoils are all of low energy and fall below the 2 keVee threshold so there is zero predicted modulation, and at very high WIMP masses, where the modulation amplitude is negative so that a good fit requires an unphysical negative cross-section, we are unable to fit the 2 bin data. Good fits can be found over a broad range of WIMP masses, ~ 2 –100 GeV, as indicated in Figure 3 and Figure 4; the latter of which includes the channeling effect. Effectively, analysis of the 2 bin data requires only a fit to the *amplitude* of the modulation spectrum, not the *shape* of the spectrum, and only weakly constrains the WIMP mass. We used here two data points and four parameters, thus the value of the minimum χ^2 , which is zero for several points in parameter space, does not provide an indication of the goodness of the fit.

The 36 bin data set breaks the full energy range into much smaller bins; the positive signal is now found in six separate bins over 2–5 keVee. To provide a good fit to the data in this case, the predicted spectra must not only have the correct *amplitude*, it must have the correct *shape* to produce the proper signal in all six of those bins. [The higher energy bins

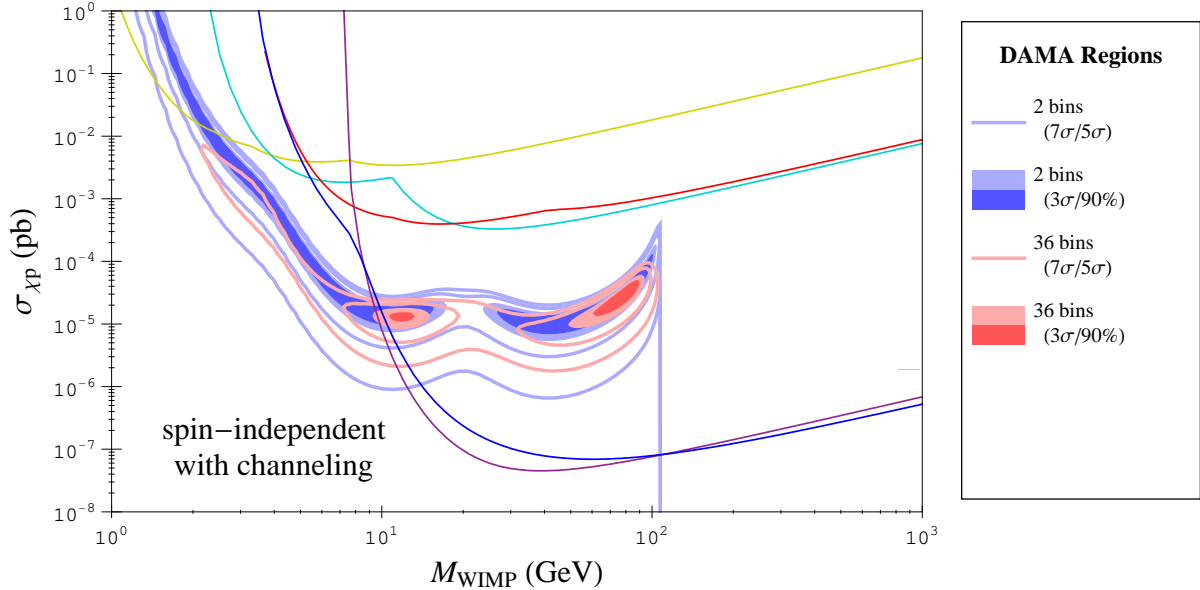


FIG. 4: Same as Figure 3, but including the channeling effect for DAMA. The 36 bin low mass region around 12 GeV is predominantly due to scatters off of I that undergo the channeling effect, as opposed to scatters off of Na as in the no ion channeling case shown in Figure 3; ordinary Na scatters and channeled I scatters coincidentally provide good fits at similar WIMP masses.

are consistent with zero modulation, but again that is typically expected for the spectra in the SHM.] Since the shape of the spectrum depends significantly on the WIMP mass, the 36 bin data set is able to much better constrain the WIMP mass than the 2 bin data set, as shown in Figures 3 & 4. The reason for the difference can more clearly be seen by the spectra in Figure 2. At a low WIMP mass of 4 GeV, the (no channeling) spectra at the best fit SI cross-section is shown in blue for 2 bins, with a χ^2 of 0.25 on 1 d.o.f., and in red for 36 bins, with a χ^2 of 87.0 on 35 d.o.f.; spectra including the channeling effect are shown in dashed lines with the same colors (with corresponding χ^2 given in the legend). At such a low WIMP mass, the spectra are very sharp and drop off rapidly as light WIMPs are not capable of inducing high energy recoils. The fit to the 2 bin data is, in fact, nearly a perfect fit to the low energy bin as the very large amplitude just above the 2 keVee threshold and small amplitude over the rest of the 2–4 keVee bin gives the correct average modulation over that bin. On the other hand, the fit to the 36 bin data is very poor: it overestimates the modulation amplitude in the first bin, but underestimates it for the next five. The *shape* of the spectra required by the 36 bin data cannot be matched at this WIMP mass. For comparison, the spectrum is shown in green for the best fit mass, near 80 GeV, which has a χ^2 of 27.1 on 34 d.o.f. This spectrum is a very good fit to both the 2 bin and 36 bin data sets.

Of note is the fact that the first (lowest energy) bin actually has a lower amplitude than the next few bins. At low enough energies, the modulation actually reverses phase and the amplitude becomes negative. The lower first bin may be an indication that the DAMA threshold is just above the energy at which the modulation reduces phase. Since that energy is dependent upon the WIMP mass, the lowest bin makes an important contribution

to constraints on the WIMP mass.

For 36 bins, there are two mass regions that allow a good fit to the data: around 10–15 GeV and 60–100 GeV, as seen in Figure 3. In the lower mass region, scattering off of Na produces a spectrum that matches the data, while in the higher mass region, scattering off of I produces the appropriate spectrum. In those two regions, scattering is also predominantly off of Na and I, respectively.

The 36 bin data will be used for the remainder of the paper.

B. DAMA Detector Effects

Energy resolution. The finite energy resolution serves to smear out the modulation spectrum. It leads to a mild improvement in sensitivity to low mass WIMPs, but is not as significant an effect as the two discussed below. The finite energy resolution is included in all our results.

Ion channeling (IC). The channeling effect reduces DAMA’s recoil energy threshold. Whereas a scattering event with the minimum observed energy of 2 keVee is conventionally assumed to be the quenched energy of a 6.7 keV recoil off of Na ($Q_{Na} = 0.3$) or a 22.2 keV recoil off of I ($Q_I = 0.09$), it could also be due to a channeled event with a true recoil energy of 2 keV. This lower recoil energy threshold provides greater sensitivity to low mass WIMPs. This is apparent when comparing the 2 bin result of Figure 4 (channeling) with Figure 3 (no channeling), as a much smaller cross-section is sufficient at low masses to produce the necessary signal in the channeling case.

There are four groups of scatters—off of Na and I, each with or without channeling—that contribute to the modulation spectrum and each of those groups will have a best fit to the data at different regions of parameter space. Whereas there were two “preferred” regions without channeling (Figure 3), there are now potentially four. Predominantly scattering off of Na and I, without channeling, should again represent a good fit to the data around 10–15 GeV and 60–100 GeV, respectively. The best fit regions to channeled scatters off of Na is at even lower masses and is apparent as the bump in the 2 bin region of Figure 4 around 2–4 GeV. However, as evident by the lack of 36 bin regions (only the 7σ contour covers that mass), channeled events off of Na do not actually provide a reasonably shaped spectrum at these light masses, even though that is where their “best” spot is. The only other region is that due to channeled events off of I. That coincidentally also occurs around 10–15 GeV, the same as unchanneled Na events. In fact, the channeled I events provide a much larger contribution to the modulation at those WIMP masses than the unchanneled Na events do, as evidenced by the reduction in the best fit cross-section by over an order of magnitude from Figure 3 to Figure 4. Thus, there are two best fit mass regions when channeling is included: a ~ 10 –15 GeV low mass region due to predominantly channeled scattering events off of I and a ~ 60 –100 GeV high mass region due to predominantly unchanneled scattering events off of I. Though the best fit masses without including channeling are nearly the same as when including this effect, that is mainly a coincidence: the low mass region in the former case is due to scatters off of Na, while the low mass region in the latter case is due to channeled scatters off of I.

Migdal effect. We do not include the Migdal effect in our analysis at this time, but we plan to include it in a future paper.

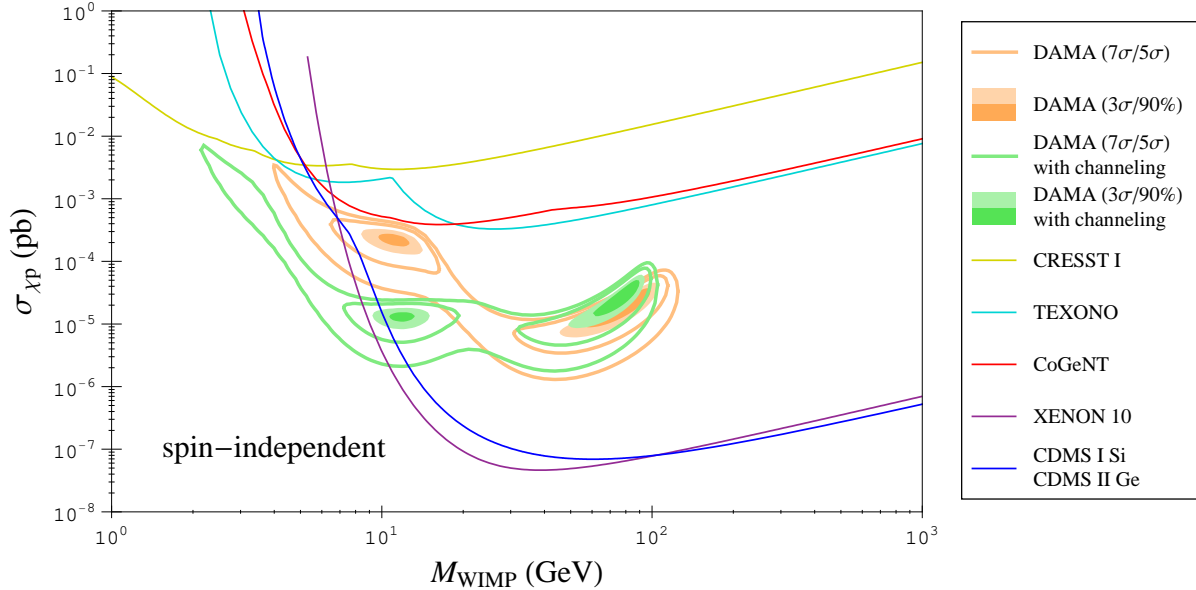


FIG. 5: Experimental constraints and DAMA best fit parameters for SI only scattering. The DAMA best fit regions are determined using the likelihood ratio method with (green) and without (orange) the channeling effect.

C. DAMA Analysis Techniques

The likelihood ratio analysis of DAMA yields a 4-dimensional confidence region over the $(m, \sigma_{p,\text{SI}}, a_p, a_n)$ parameter space. In Figures 5, 6, and 7, we show the SI only ($a_p = a_n = 0$), SD proton-only ($\sigma_{p,\text{SI}} = a_n = 0$), and SD neutron-only ($\sigma_{p,\text{SI}} = a_p = 0$) slices of this confidence region, respectively, with (green) and without (orange) the channeling effect. Later, we will show slices in other, mixed coupling cases. This analysis indicates the parameters most likely to produce the DAMA signal. If some 2-dimensional plane in the full parameter space allows for only a poor fit relative to the best fit point (the global χ^2 minimum), there will be no slice in that plane. The fact that we have found slices in all of the SI only, SD proton-only, SD neutron-only, and mixed SD coupling cases is an indication that each of these cases is a relatively reasonable possibility for producing the DAMA signal. That is, even though we allow for mixed SI and SD couplings, the DAMA signal can still reasonably be produced by SI only scattering; the same may be said of the other coupling possibilities. One may see this from the minimum χ^2 given in Table IV: although the SI only case provides a mildly lower χ^2_{min} (27.1 without channeling) than that the SD cases (29.3–31.0), they are all very similar to the global minimum (27.1).

By finding a 4-dimensional confidence region, direct comparisons and (to some degree) interpolations may be made between the DAMA regions of different coupling cases. Alternatively, we could have considered each case to be its own 2 parameter model in (m, σ) , where σ represents the type of cross-section in that case (*e.g.* $\sigma_{p,\text{SI}}$), and found the corresponding 2-dimensional confidence regions. However, each analysis would be based on a different theoretical framework and would not be statistically correlated; one must then be cautious when making comparisons between, *e.g.*, the resulting SD proton-only and SD neutron-only

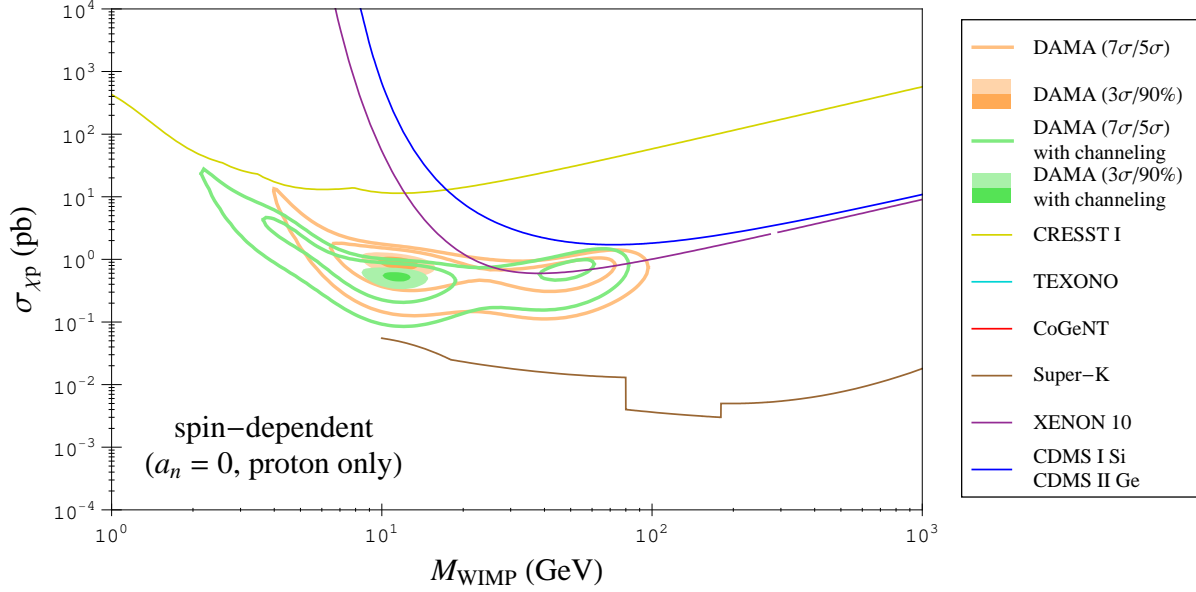


FIG. 6: Experimental constraints and DAMA best fit parameters for SD proton-only scattering. The DAMA best fit regions are determined using the likelihood ratio method with (green) and without (orange) the channeling effect. The CoGeNT and TEXONO constraints are too weak to fall within the shown region.

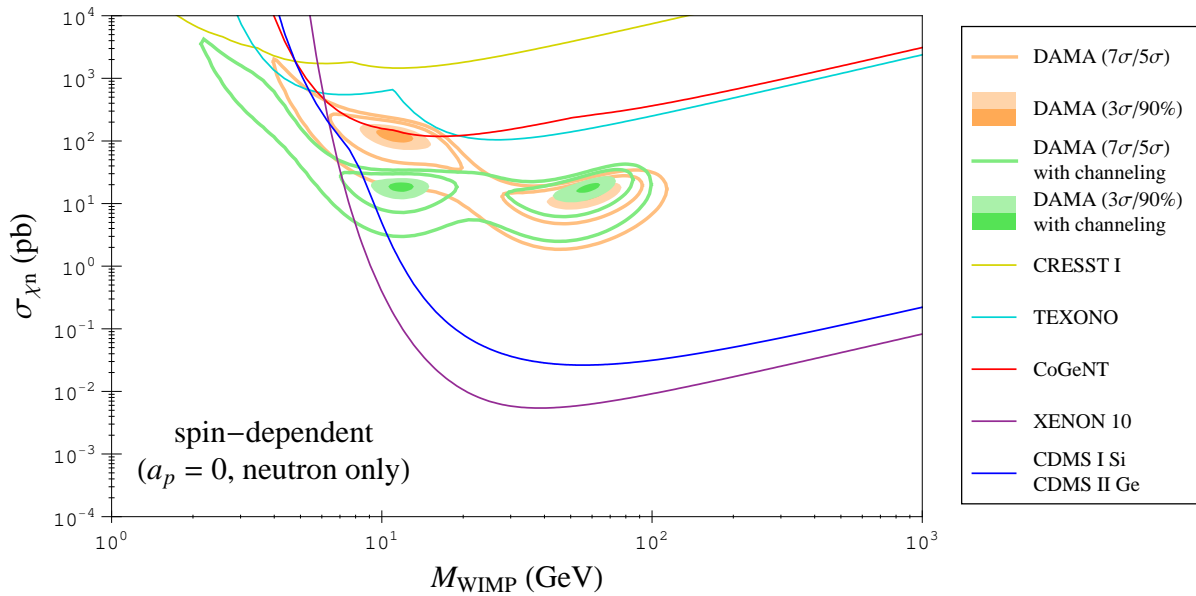


FIG. 7: Experimental constraints and DAMA best fit parameters for SD neutron-only scattering. The DAMA best fit regions are determined using the likelihood ratio method with (green) and without (orange) the channeling effect. Super-Kamiokande (SuperK) provides no constraints in this case and is not shown.

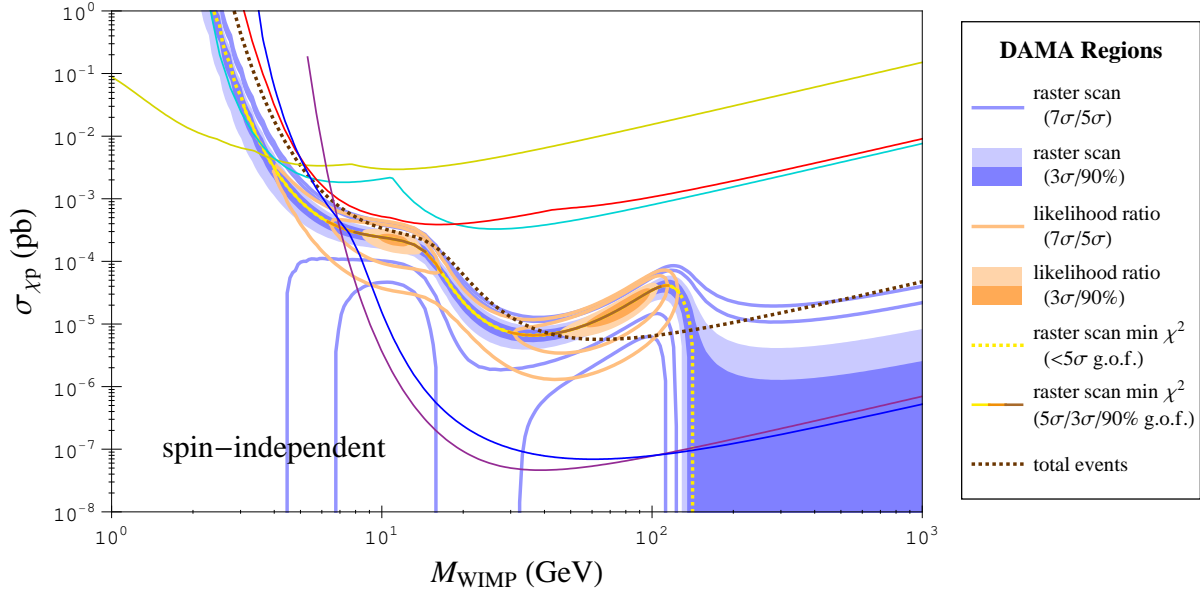


FIG. 8: Two statistical analyses of DAMA (best fit and raster scan) vs. null results of other experiments for SI scattering. DAMA best fit regions (likelihood analysis) are shown by the orange regions (90%/3 σ) and contours (5 σ /7 σ). [Technically, these regions are the 2D $a_p = a_n = 0$ slices of the full 4D confidence region as described in the text.] The blue bands and contours are raster scans over the WIMP mass, corresponding to the most likely cross-sections at each WIMP mass. The data is not used to constrain the WIMP mass in a raster scan analysis; however, the brown/orange/yellow line shows the cross-section that minimizes the χ^2 (best fit cross-section) at each mass, with the color indicating a goodness-of-fit within the 5 σ /3 σ /90% level at those cross-sections (dotted yellow indicates a goodness-of-fit below 5 σ , a very poor fit). Null experiment constraints are as described in Figure 5. The constraint imposed by the total event rate in DAMA (as opposed to the modulation) is shown by the dark dotted curve. The likelihood ratio analysis is decoupled from a goodness-of-fit test and the lack of an overlap between the DAMA best fit regions (as determined by the likelihood ratio) and the allowed regions of other experiments does not, by itself, indicate an incompatibility between the experiments. Such comparisons, however, may be made using the χ^2 goodness-of-fit contours shown in Figure 10. The constraint due to the total event rate in DAMA (dotted line) shows that some parameters that yield the correct modulation amplitude predict too many total events and are therefore excluded.

confidence regions. In theory, such 2-dimensional confidence regions may be very different from the slices of the 4-dimensional confidence region. In practice, for the coupling cases considered here, they turn out to be somewhat similar, which is a consequence of the similar χ_{\min}^2 in the different cases.

As discussed previously, there are generally two preferred WIMP mass ranges: a low mass range ~ 10 – 15 GeV (due to scatters primarily off of Na or channeled I scatters, when channeling is included) and a high mass range ~ 60 – 100 GeV (due to scatters primarily off of I). Low, high, and intermediate WIMP masses generally produce worse fits (though not necessarily *bad* fits). Previous analyses have found low WIMP masses, below these preferred ranges, to be of interest. In addition, the LHC or other (non-direct detection) experiments,

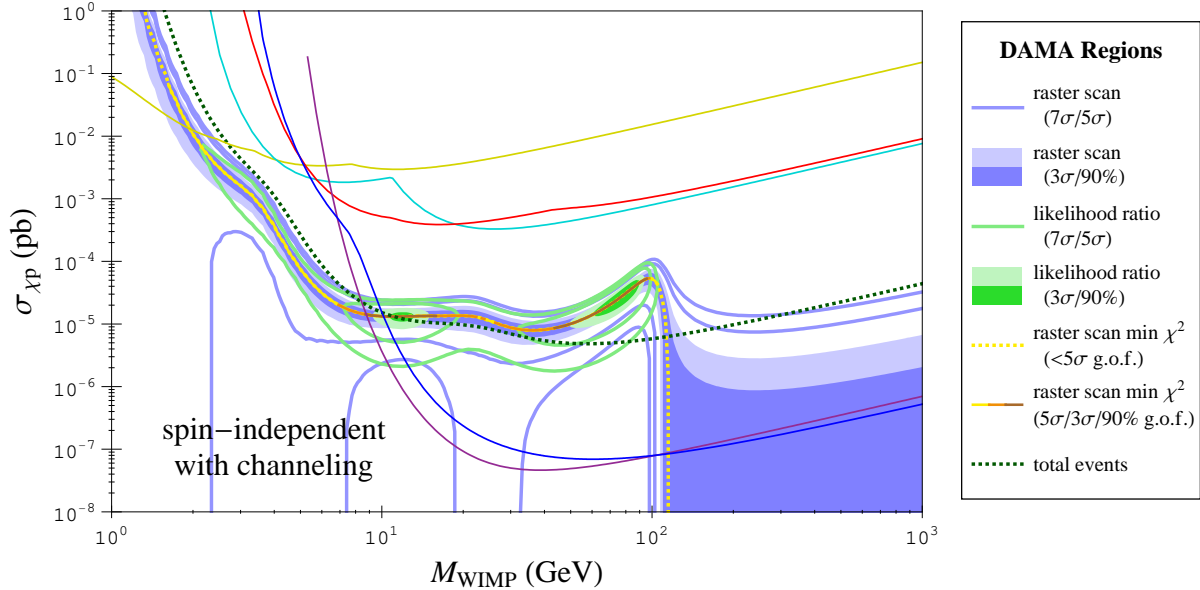


FIG. 9: Same as Figure 8, but including the channeling effect for DAMA.

if they observe *e.g.* neutralinos, might be able to provide the mass of the WIMP. For these cases, it is useful to use the raster scan, which does not use the data to make assumptions on the WIMP mass and provides appropriate confidence intervals in the scattering cross-section for a given (known) WIMP mass.

The raster scan is shown in Figure 8 (without channeling) and Figure 9 (with channeling) for SI only scattering. Regions shown in dark/light blue are the confidence regions at 90%/3 σ C.L., while the light blue contours indicate the confidence regions at a 5 σ /7 σ C.L. (the outer contour is 7 σ). For comparison, the DAMA likelihood ratio regions and null experiment constraints are also shown; these regions and constraints are equivalent to the ones shown in Figure 5. The raster scan regions pass through the likelihood ratio regions (as should be expected). At masses where the raster scan regions/contours extend to the bottom of the figure (7 σ /5 σ at low masses, 7 σ at intermediate masses, and for all C.L.'s at high masses), the regions actually extend all the way to a zero cross-section, *i.e.* a cross-section of zero falls within the corresponding C.L. at those masses.

The brown/orange/yellow line along the raster scan indicates the best fit cross-sections (minimizing the χ^2) at each WIMP mass. At a particular mass, the reasonableness of the best fit cross-section (and corresponding confidence interval) may be tested against the χ^2 distribution with 35 d.o.f. (36 bins with a fit to one parameter): the brown/orange/yellow color of the line indicates the best fit cross-section at that mass falls within a 90%/3 σ /5 σ probability level (dotted yellow is below 5 σ). Changes in the color often occur near one of the likelihood ratio contours; this is only coincidental as the two types of regions use different statistical methods and are not in direct correspondence.

The most appropriate use of the raster scan is if one has an interest in a particular WIMP mass (or specific range of WIMP masses): the raster scan indicates the confidence interval (most preferred or best fit values) in the cross-section at that mass and the color of the

central line indicates the goodness-of-fit of that particular model/interval ⁵. If there is no interest in specific WIMP masses, the likelihood ratio method should be used instead.

The regions determined using the likelihood ratio and raster scan methods indicate the best fit parameters for producing the DAMA signal, assuming that signal is actually produced by some particular set of parameters in the assumed theoretical framework. These analyses, however, are decoupled from the goodness-of-fit: the resulting regions do not indicate if those parameters are a good fit to the data or a poor one (which may indicate the assumed theoretical framework, *e.g.* the SHM, is incorrect). That is, the best fit parameter regions are not equivalent to the regions that provide a good fit to the data. Some parameters that fall outside of the best fit regions may actually provide reasonably good fits to the data (just not as good as parameters within the region), while some parameters inside the best fit regions may provide poor fits to the data (just not as bad as parameters outside the region). In the likelihood ratio method, only one of these two cases is possible, depending upon the value of χ^2_{\min} , *i.e.* there will be either good fits outside the region or bad fits within, but not both.

Because these two regions indicate best fit parameters, but not the “allowed” parameters, they should not be used to determine the compatibility with other experiments. For example, in the SI case with channeling shown in Figure 5, the XENON10 constraint essentially rules out the 4σ DAMA likelihood ratio best fit parameter region (not shown, but falls midway between the 3σ and 5σ regions). However, at about $m = 8$ GeV and $\sigma_{p,SI} = 10^{-5}$ pb, the predicted recoil and modulation spectra are compatible with XENON10 and DAMA at about the 90% and 2σ levels, respectively, using a χ^2 distribution for the latter.

The best way of determining the compatibility of the various experiments is to do a combined analysis, such as a likelihood ratio analysis, that takes into account all the available experimental data ⁶. However, this is fairly difficult to do due to the wide range of analyses used by the various experiments and the lack of background subtraction makes it even more difficult (the likelihood is ill defined in this case). Rather, we will more conservatively compare experiments using a χ^2 goodness-of-fit (g.o.f.) test for DAMA for each set of parameters (there is no fit to the parameters, so we use a χ^2 distribution with 17 d.o.f., recalling the high energy bins have been combined for the g.o.f. test). The χ^2 g.o.f. regions are shown as black contours in Figure 10 (without channeling) and Figure 11 (with channeling) where the DAMA data is compatible with the predicted spectrum at the 90%, 3σ , and 5σ level. Parameters outside those contours are incompatible with the data at at least the corresponding level; these contours are constraints on the parameter space. These contours are appropriate for comparing DAMA with the other experiments since, if a set of parameters provides a poor fit to the data of one experiment, including DAMA, it almost certainly will be a poor fit in a combined analysis as well. These χ^2 g.o.f. contours are a conservative means of examining the compatibility as a combined analysis could possibly provide stronger constraints, but is unlikely to provide more lenient constraints.

As they are both determined from the χ^2 of the data, the contours for the likelihood

⁵ A technical point: the raster scan confidence region is the band of confidence intervals over *all* masses. The goodness-of-fit test at the best fit cross-section at a given mass is only a test of the confidence interval at that mass. If this test is used to “cut” the band at some WIMP masses, the resulting region would not formally be a confidence region.

⁶ The best fit parameter region determined via the likelihood ratio method may shift significantly with these other experimental constraints added, yet still provide a reasonable fit to the data.

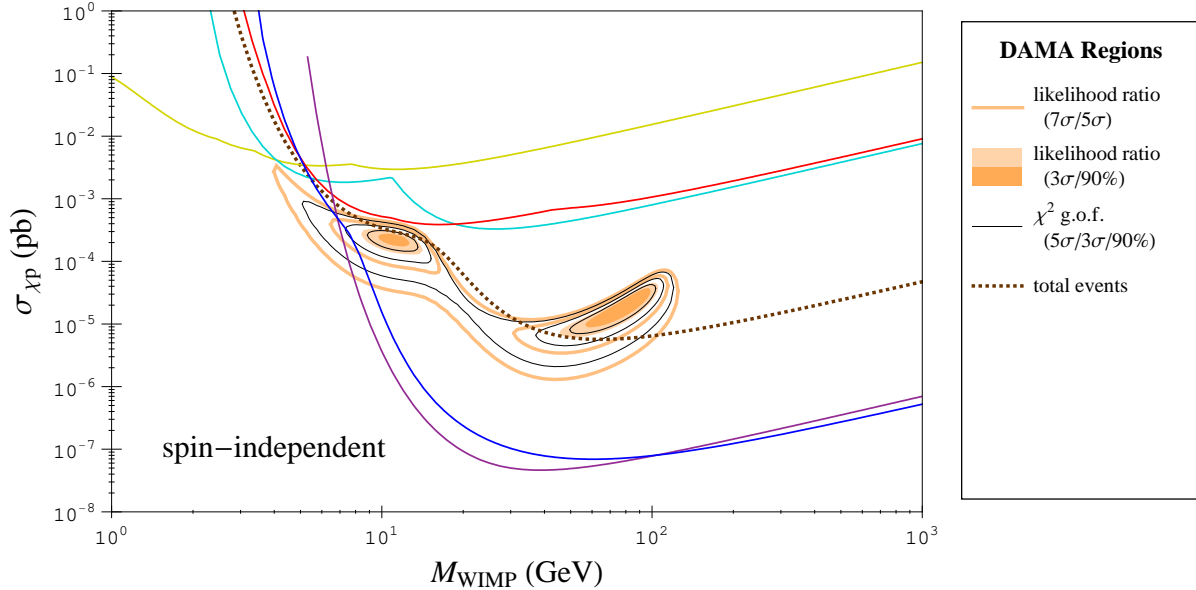


FIG. 10: Two statistical analyses of DAMA (best fit and goodness-of-fit (g.o.f.)) vs. null results of other experiments for SI scattering. The best comparison with other experiments is via the g.o.f. regions shown here. The most likely parameters to produce the DAMA signal, as determined using the likelihood ratio method, are indicated by the orange regions (90%/3 σ) and contours (5 σ /7 σ). The black contours correspond to a conservative χ^2 g.o.f. test to the DAMA data. The constraint imposed by the total event rate in DAMA is shown by the dotted curve. Null experiment constraints are as described in Figure 5. Both DAMA regions shown are based on the χ^2 value and thus have similar contours shapes, but they have different χ^2 cutoffs at a given confidence level and are not equivalent; *e.g.* the 5 σ likelihood ratio contour is nearly the same as the 3 σ g.o.f. contour. Direct comparisons between DAMA and the other experiments should be done using the χ^2 g.o.f. regions, not the likelihood ratio regions.

ratio and g.o.f. methods are similar in shape, as can be seen in Figures 10 & 11. However, the χ^2 corresponding to a given C.L. is different in the two methods. In particular, while some contours of the likelihood ratio analysis seem to closely match contours of the χ^2 g.o.f. analysis, they are not of the same level. For example, the 5 σ likelihood ratio contour is very similar to the 3 σ g.o.f. contour.

To summarize, the choice of the DAMA analysis method to use should be the following: if the most likely parameters to produce the DAMA signal are desired, use the likelihood ratio; if interested in a *particular* WIMP mass or range of masses, use the raster scan; and if direct comparisons (particularly, the compatibility) are to be made with other experiments, use the χ^2 g.o.f. analysis.

D. DAMA Total Rate

The total event rate in DAMA imposes constraints on the DAMA compatible parameter space; this total rate constraint is shown as a dotted curve in Figure 8 and the following

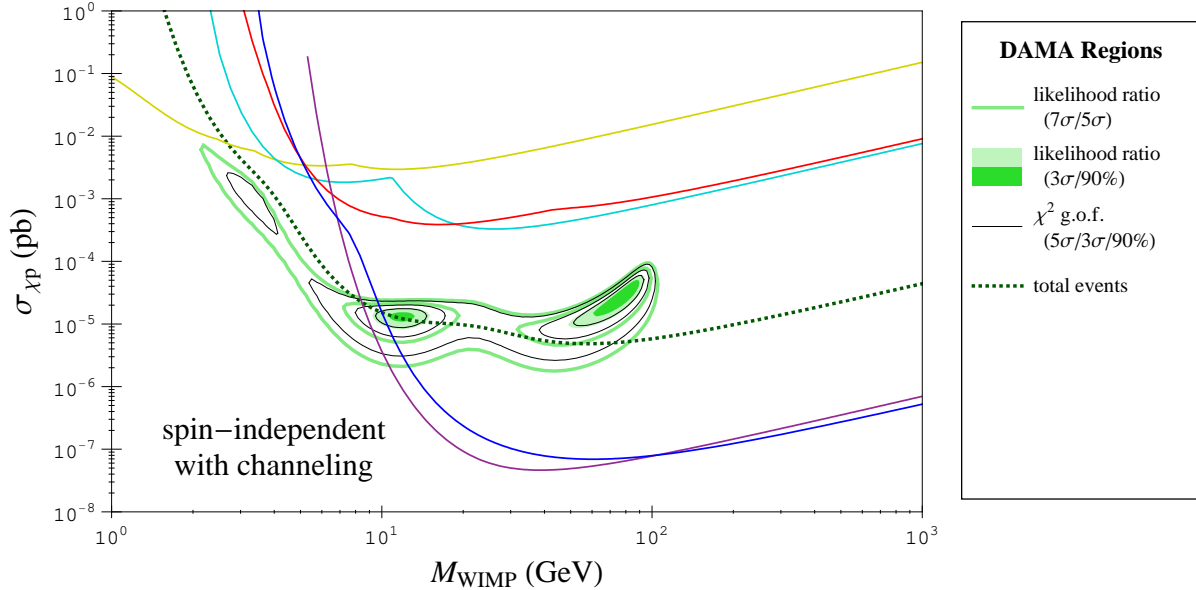


FIG. 11: Same as Figure 10, but including the channeling effect for DAMA.

figures. Parts of parameter space that would produce the DAMA modulation signal, such as the higher WIMP mass regions for the SI case shown in Figure 10 (without channeling) and Figure 11 (with channeling), predict far more total events in the DAMA detector than observed and are therefore ruled out as an explanation for the DAMA signal.

In general, the total rate provides a strong constraint for the higher WIMP mass region that is favorable for the modulation signal in the various coupling cases, excluding the 90% (without channeling) and 3 σ (with channeling) g.o.f. regions. Thus, high mass WIMPs are disfavored as the source of the DAMA signal for the models considered here. The lower WIMP mass regions, however, are only minimally constrained by the total rate in DAMA.

E. Spin-Independent Scattering

The DAMA best fit parameters and null experiment constraints for SI only scattering are shown Figure 5 both with (green) and without (orange) channeling for DAMA. Channeling greatly reduces the scattering cross-sections necessary to produce the DAMA signal in the lower WIMP mass region (~ 9 – 15 GeV) and opens up even lower mass regions (down to ~ 2 GeV), albeit only at a very low 7 σ C.L. CDMS and XENON10 exclude all the 3 σ C.L. best fit regions. The low exposure experiments—CoGenT, CRESST I, and TEXONO—do not quite constrain the DAMA best fit regions. Both our older analyses and those performed by some of the experimental groups indicate these experiments *do* constrain portions of the DAMA region, but there are several differences between those analyses and our analysis here that change the DAMA best fit region (aside from any potential conservative assumptions on the experimental data sets as described in Section III): (1) an increase in the number of DAMA data bins from 2 to 36; (2) inclusion of DAMA’s finite energy resolution, which increases the number of scatters over threshold and reduces the necessary cross-section, particularly at lower WIMP masses; (3) inclusion of the channeling effect, where indicated;

and (4) no background subtraction. Aside from shifting the DAMA best fit region downward, these changes lead to the very low mass regions disappearing from the best fit confidence regions, where the low threshold experiments provide the strongest constraints. SuperK provides relatively weak constraints for this SI case.

The best fit SI cross-sections at low WIMP masses are indicated by the raster scan regions in Figure 8 (without channeling) and Figure 9 (with channeling). Without channeling, CRESST I and, to some degree, TEXONO constrain the 3σ best fit cross-sections at masses below about 3 GeV. The best fit cross-section at these masses presents a poor fit to the DAMA data: they are incompatible at at least the 5σ level. With channeling included, the best fit cross-sections shift downwards at these low masses and are no longer constrained by TEXONO. CRESST I excludes the best fit cross-sections only below ~ 1.5 GeV in this case. At high WIMP masses (above ~ 100 GeV), with and without channeling, the best fit cross-section is actually zero. The reason for this is that, for heavy WIMPs, the lowest energy bins will actually have a negative modulation amplitude, whereas the observed amplitude is positive. The best fit cross-section would then be an unphysical negative value; the best physically allowed value is zero. As at very low masses, the best fit cross-sections at these high masses represent poor fits to the DAMA data (incompatible at $> 5\sigma$).

To examine the compatibility of DAMA with other experiments, we use the χ^2 g.o.f. regions shown in Figure 10 (without channeling) and Figure 11 (with channeling). Without channeling, CDMS and XENON10 exclude all the parameter space that is compatible with the DAMA data within the 3σ level. With channeling, CDMS and XENON10 exclude all the parameter space that is compatible with the DAMA data within the 90% level. There are parameters at 8–9 GeV that are compatible with DAMA within the 3σ level and still satisfy the other constraints. Lower masses, while not constrained by the null experiments or DAMA’s total rate, are only compatible with the DAMA data below the 3σ level.

We note that these results are sensitive to the thresholds of the two large exposure experiments, CDMS and XENON10. In particular, the DAMA 3σ g.o.f. region with channeling would have been excluded with the use of the original \mathcal{L}_{eff} value of 0.19 for XENON10, instead of the more recent measurement of 0.14 (which shifted the XENON10 threshold from 4.6 keV to 6.1 keV). The small window of compatibility at low WIMP masses is thus very dependent on the calibrations of these experiments’ detectors. Given the closeness of the upward turn-off in the CDMS and XENON10 constraints (due to their thresholds) with the low mass DAMA region, even small adjustments to the calibrations, which will shift the turn-off in the constraints to slightly higher (or lower) WIMP masses, may open up more of the DAMA low mass region (or exclude it completely).

F. Spin-Dependent Scattering

We here present results for the case of purely spin-dependent interactions. We study the cases of scattering off of protons only, neutrons only, and mixed proton & neutron scattering.

1. Proton-Only

For the SD proton-only scattering case ($a_n = 0$), the DAMA best fit parameters and null experiment exclusion limits are shown in Figure 6. Unlike the SI case (and the SD neutron-only case to be examined below), there is no high mass best fit region at better than a 5σ

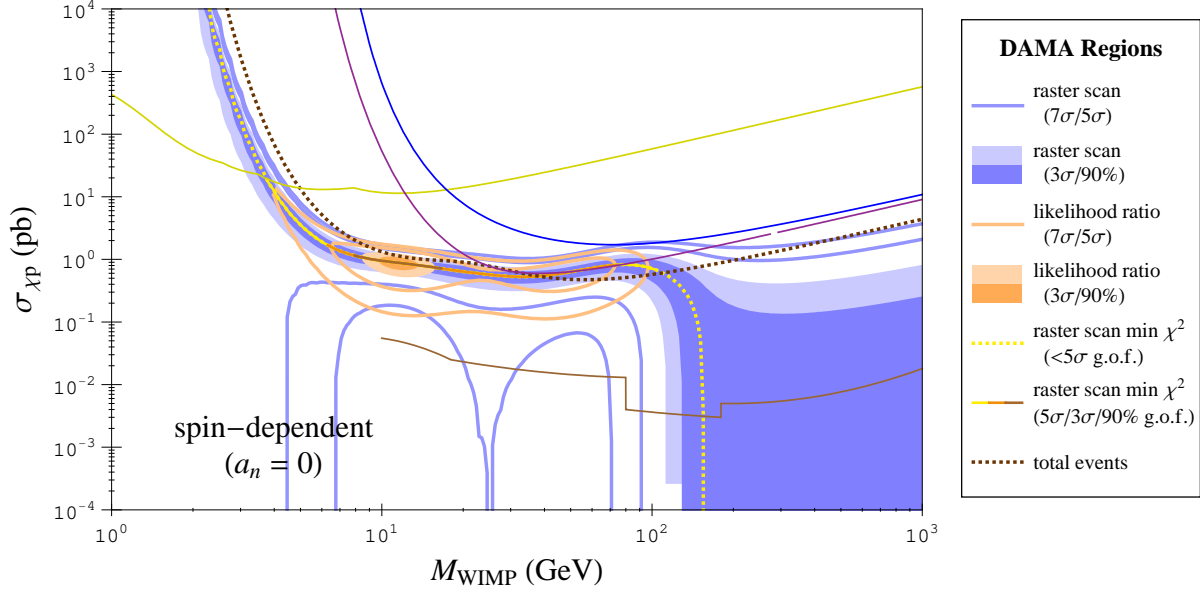


FIG. 12: Experimental constraints and DAMA best fit parameters for spin-dependent (SD) proton-only scattering. The DAMA raster scan and likelihood ratio regions are as described in Figure 8. Null experiment constraints are as given in Figure 6.

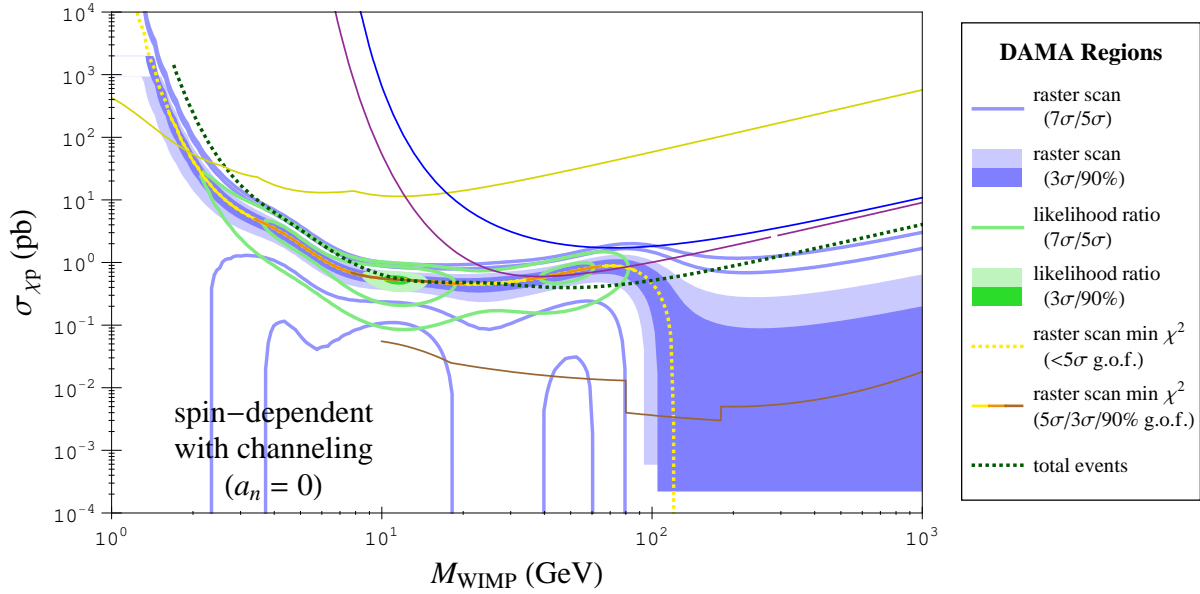


FIG. 13: Same as Figure 12, but including the channeling effect for DAMA.

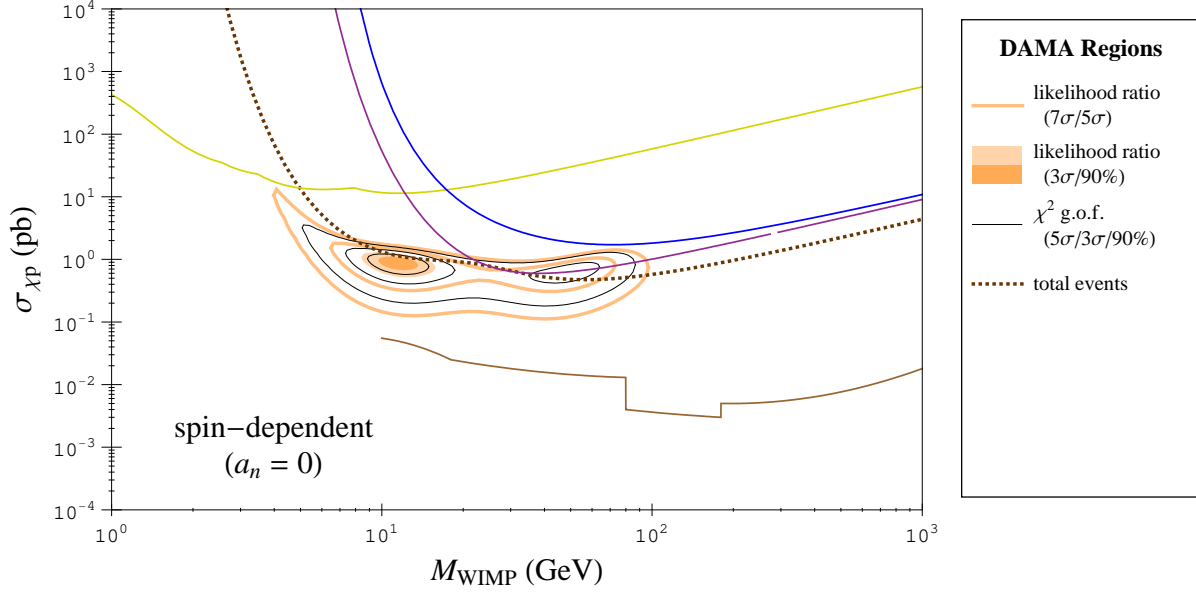


FIG. 14: Experimental constraints and DAMA best fit parameters for spin-dependent (SD) proton-only scattering. The DAMA raster scan and χ^2 g.o.f. regions are as described in Figure 10. Null experiment constraints are as given in Figure 6.

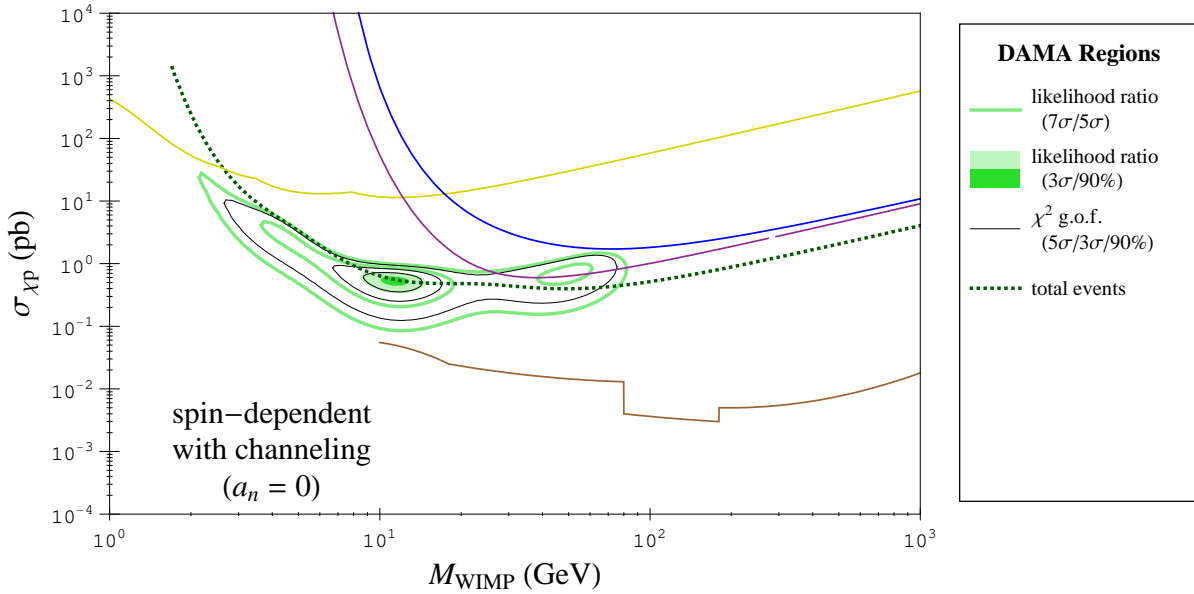


FIG. 15: Same as Figure 14, but including the channeling effect for DAMA.

C.L.; the best fits are strictly found around 11 GeV. The addition of channeling does not reduce the cross-sections of the best fit region as much as in other cases. These differences are a result of the relatively small contribution from scatters off of I in this case: where I presents the best fit to the DAMA data (the high mass region), there are enough Na scatters (which do not match the observed spectrum at those masses) to make the total spectrum a relatively poor fit, thus eliminating the higher mass region found in other cases at the 90% & 3σ C.L.'s. The relatively small amount of I scatters means less of the channeled I scatters, which contribute to the low mass region, so the low mass region does not shift to much lower cross-sections.

Constraints from experiments with proton-even detector materials (*e.g.* Si, Ge, and Xe) are significantly weakened as those elements have very little spin in their proton groups for a WIMP to couple to. Notably, CoGeNT and TEXONO (both Ge) constraints are too weak to appear in the various SD proton-only figures. CDMS and XENON only mildly constrain the 5σ and 7σ C.L. DAMA best fit regions at higher WIMP masses. CRESST I, which uses proton-odd Al, still has reasonably strong constraints, but these fall just outside the 7σ C.L. DAMA best fit region. SuperK, on the other hand, strongly constrains all of the DAMA best fit regions above their analysis threshold of 10 GeV. Only a small portion of the 3σ C.L. region survives around 9–10 GeV, but would almost certainly be excluded if SuperK extended their analysis to lower masses. If any of the assumptions required for analyzing indirect detection limits from high energy solar neutrinos does not hold (see Section III), so that the SuperK constraint does not apply, nearly all the the DAMA best fit parameter space survives in this case.

Not shown in the figures are other proton-odd experiments such as COUPP [10, 11] and KIMS [14] that can provide additional constraints in this SD proton-only scattering case. As noted in Section III, COUPP does not present their results in a way that allows us to perform our own analysis and, hence, has not been included here. Both COUPP and KIMS would exclude the higher WIMP mass regions compatible with DAMA. However, KIMS has a relatively high threshold and cannot constrain the low WIMP mass DAMA region. COUPP could potentially constrain some of this low mass region, although without a reanalysis it is unclear to what degree (if it all) COUPP actually constrains the DAMA regions at these low WIMP masses.

The best fit SD proton-only cross-sections at each mass are indicated by the raster scans in Figure 12 (without channeling) and Figure 13 (with channeling). CRESST I strongly constrains some of the raster scan band at low masses (<3 GeV) without channeling and only mildly constrains that band at low masses with channeling. Again, the best fit cross-sections at those low masses, as well as very high masses, are a poor fit to the data.

Parameters compatible with the DAMA data are indicated by the χ^2 g.o.f. regions shown in Figure 14 (without channeling) and Figure 15 (with channeling). Regions compatible with each experiment at the 90% level are found at 8–10 GeV both with and without channeling ⁷. In addition, regions compatible with DAMA within the 3σ level can be found that satisfy the DAMA constraint at 7–10 GeV, or as low as 6–10 GeV when channeling is included. Without the SuperK constraint, parameters compatible with DAMA within the 90% level can be found over 8–15 GeV. Within the 3σ level, that range expands to 7–19 & 35–55 GeV

⁷ A cautionary note: saying parameters are consistent with each experiment at *e.g.* the 90% level is not equivalent to saying the experiments are consistent within the 90% level. The latter is a statement of a combined analysis, which is not performed here.

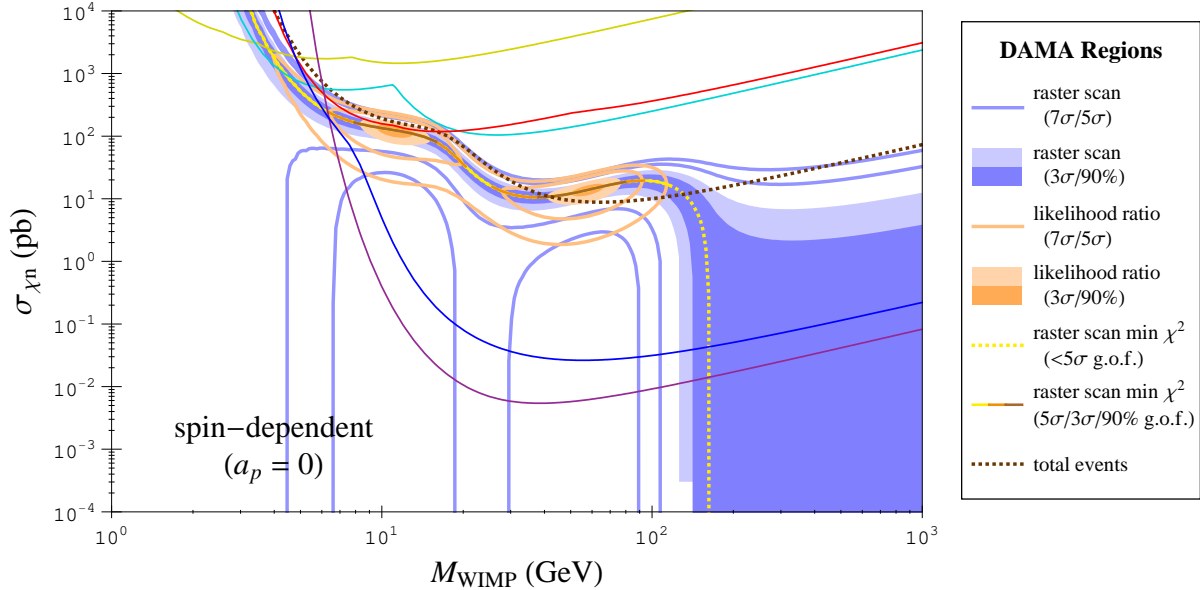


FIG. 16: Experimental constraints and DAMA best fit parameters for spin-dependent (SD) neutron-only scattering. The DAMA raster scan and likelihood ratio regions are as described in Figure 8. Null experiment constraints are as given in Figure 7.

(no channeling) or 6–18 GeV (with channeling), where some of the compatible regions have been limited by DAMA’s total event rate. However, the high mass (35–55 GeV) DAMA compatible region without channeling would be incompatible with the COUPP and KIMS experimental constraints.

2. Neutron-Only

In the SD neutron-only coupling case ($a_p = 0$), there is again two best fit mass regions, as shown in Figure 7. The addition of the channeling effect shifts the best fit cross-sections in the low mass region to lower values. For this neutron-only coupling case, experiments with the neutron-odd isotopes (*e.g.* Si-29, Ge-73, Xe-129, and Xe-131) are expected to gain in sensitivity relative to DAMA, which has only neutron-even isotopes (Na-23 and I-127). The CDMS and XENON10 constraints exclude the 5σ C.L. DAMA best fit region with and without scattering. CoGeNT also constrains some of the 3σ C.L. DAMA best fit region. Only DAMA best fit regions below a 5σ C.L. survive the other experimental constraints. SuperK provides no constraints in this case.

Once again, the DAMA best fit SD neutron-only cross-sections at each mass are indicated by the raster scans regions, shown in Figure 16 (without channeling) and Figure 17 (with channeling). The best fit cross-sections within a 3σ C.L. are excluded by CRESST I for masses below 3 GeV and by CDMS and XENON10 for masses above 7 GeV; TEXONO constrains some of the best fit cross-sections at WIMP masses in between. For masses of 3–7 GeV, the best fit cross-sections are consistent with the DAMA data only within the 3σ – 5σ level.

Parameters compatible with the DAMA data are indicated by the χ^2 g.o.f. regions shown

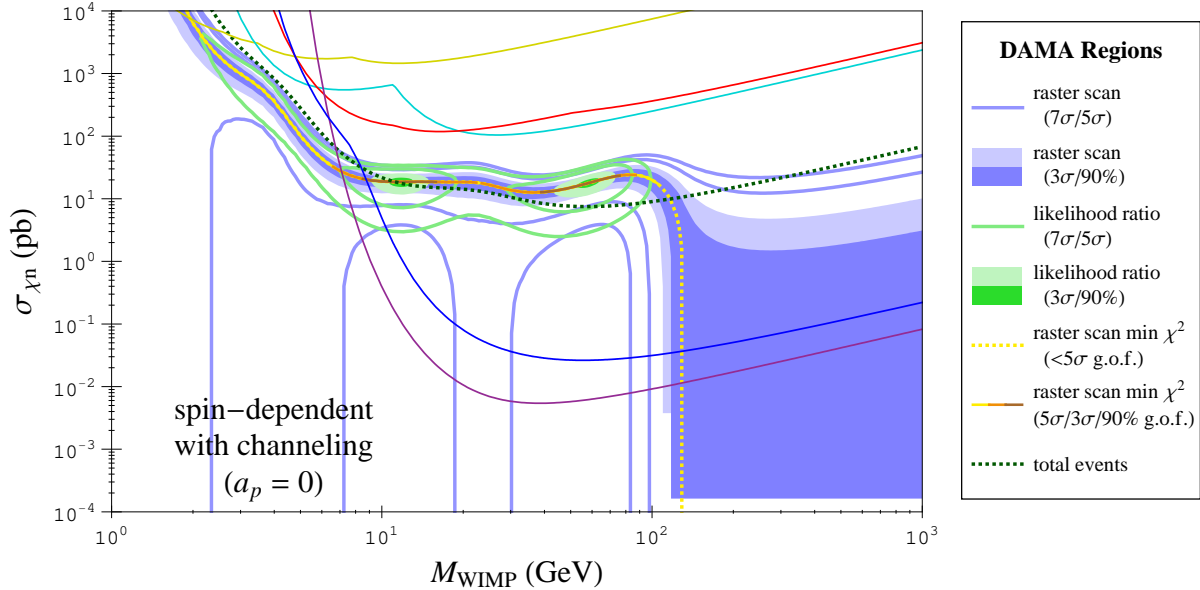


FIG. 17: Same as Figure 16, but including the channeling effect for DAMA.

in Figure 18 (without channeling) and Figure 19 (with channeling). Parameters compatible with the DAMA data within the 3σ level are excluded by the CDMS and XENON10 constraints both with and without channeling.

3. Mixed Couplings

While the previous two cases took one of the two SD couplings to be zero, there is little reason to suspect one of the couplings to be significantly smaller than the other. Now we will consider the case of arbitrary SD couplings, where both couplings may be non-zero. We show in Figure 20 the experimental constraints and DAMA best fit parameters (WIMP mass and SD WIMP-proton cross-section) in the case of equal SD couplings ($a_n = a_p$) and in Figure 21 for $a_n = -a_p$. In both cases, the SD scattering cross-sections off of the proton and neutron are equal. The null experiment constraints are nearly the same in both cases, but the DAMA best fit regions have some differences. In the $a_n = -a_p$ case, as compared to the $a_n = a_p$ case, the inclusion of channeling does not lower the best fit cross-sections in the low mass region by as much and the the higher mass region falls under a weaker C.L. As with the previous cases, we find DAMA best fit regions within a 3σ C.L. survive other constraints at WIMP masses of $\sim 8-10$ GeV. Those regions fall within the 90% χ^2 g.o.f. DAMA compatibility region (not shown), so there are parameters in these two cases that are compatible with each of the experiments within the 90% level.

In Figure 22, we show the DAMA best fit couplings in the a_p - a_n plane, along with null experiment constraints, at several different WIMP masses; SuperK constraints have not been included. The gray regions indicate the regions allowed by the various null experiments, while the green and orange regions indicate the parameters most preferred (at a 3σ C.L.) for producing the DAMA signal with and without channeling, respectively (there is no DAMA best fit region at a WIMP mass of 5 GeV). The parameters in the overlapping regions (shown

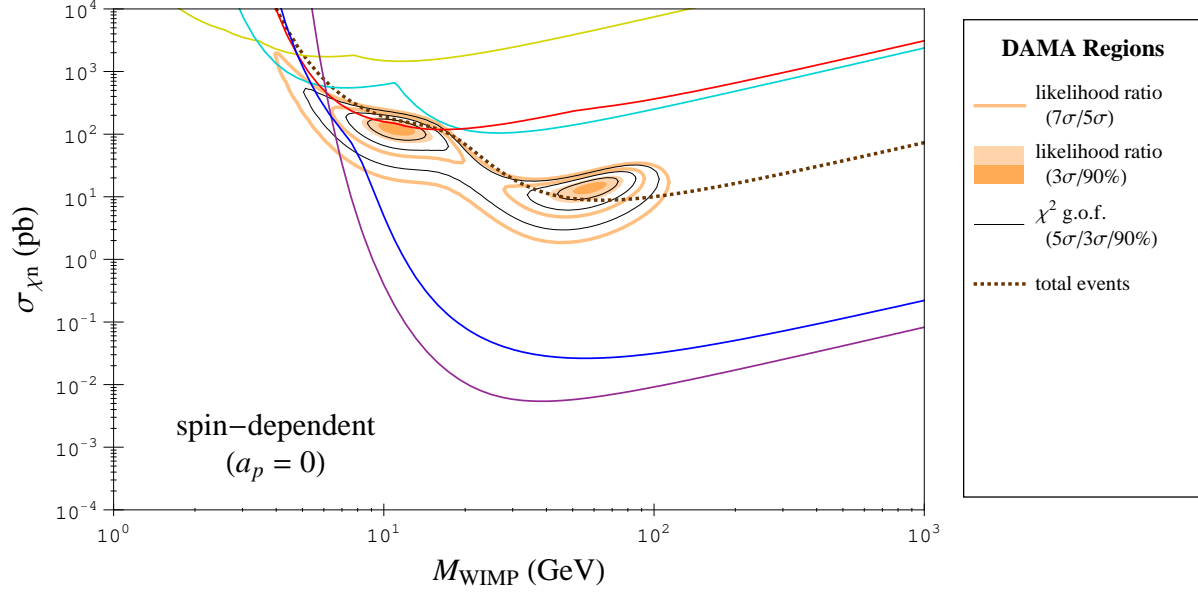


FIG. 18: Experimental constraints and DAMA best fit parameters for spin-dependent (SD) neutron-only scattering. The DAMA raster scan and χ^2 g.o.f. regions are as described in Figure 10. Null experiment constraints are as given in Figure 7.

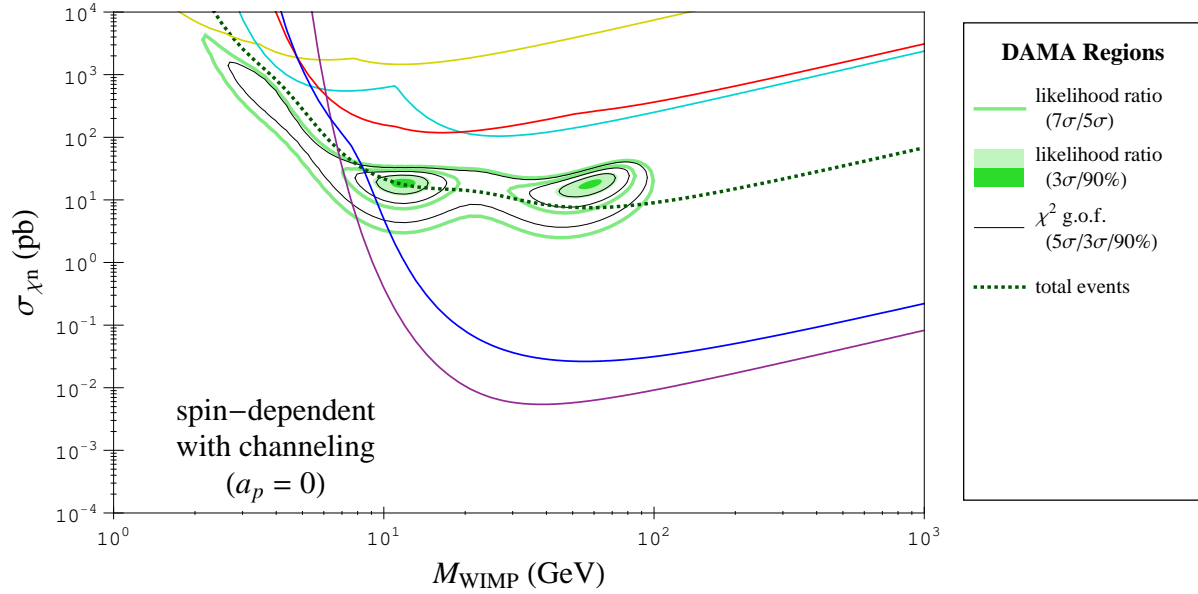


FIG. 19: Same as Figure 18, but including the channeling effect for DAMA.

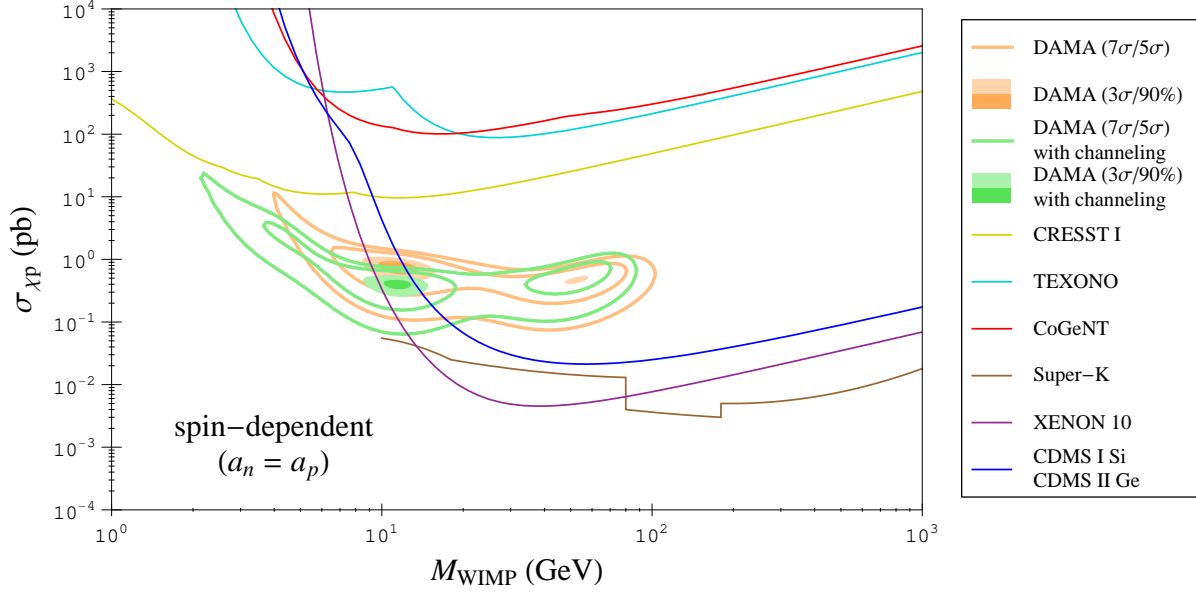


FIG. 20: Experimental constraints and DAMA best fit parameters for SD only scattering in the case $a_n = a_p$. The DAMA best fit regions are determined using the likelihood ratio method with (green) and without (orange) the channeling effect.

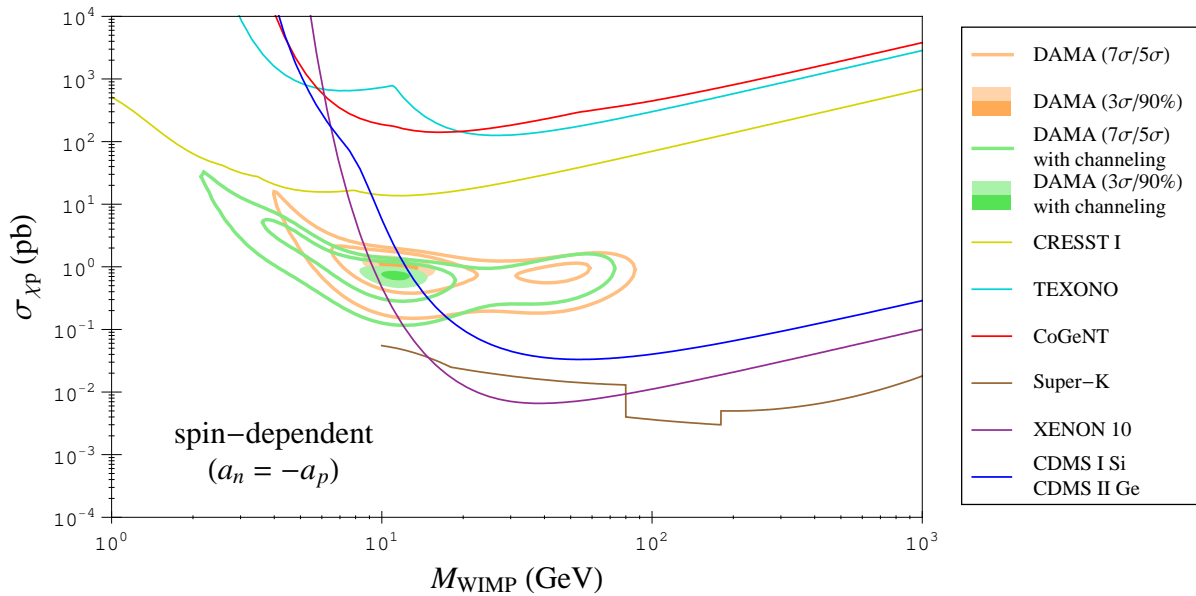


FIG. 21: Experimental constraints and DAMA best fit parameters for SD only scattering in the case $a_n = -a_p$. The DAMA best fit regions are determined using the likelihood ratio method with (green) and without (orange) the channeling effect.

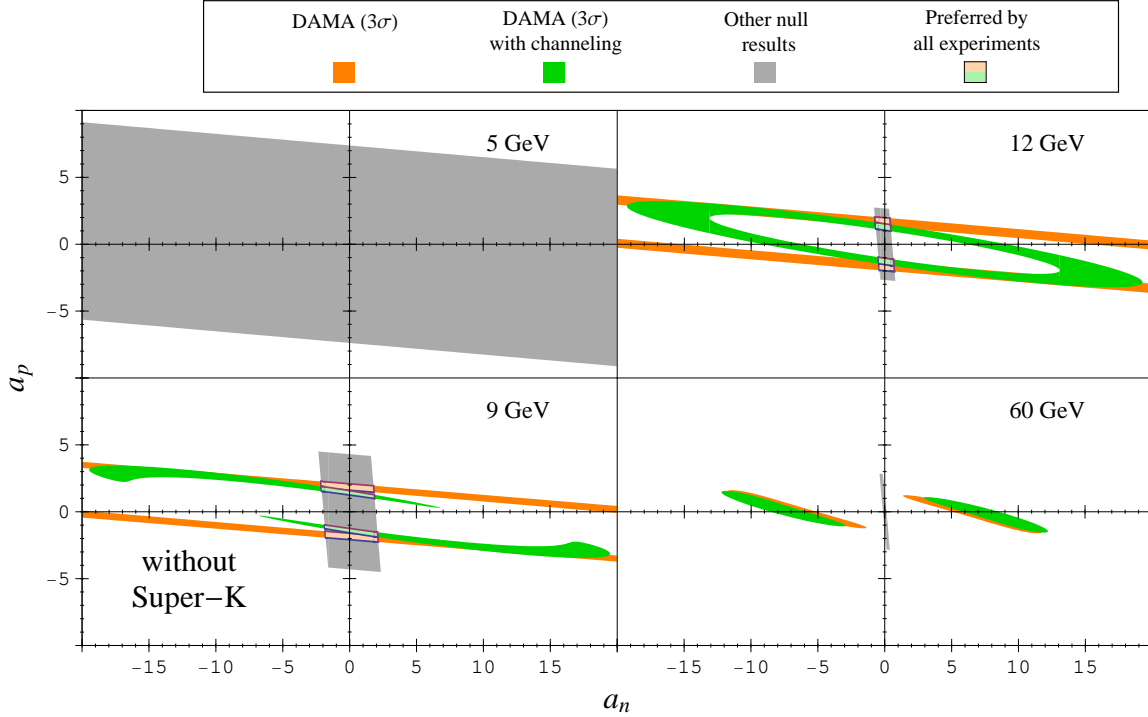


FIG. 22: Experimental constraints and DAMA best fit parameters for SD only scattering in the a_p - a_n plane at several different WIMP masses. The 3σ best fit DAMA parameters are shown in orange (no channeling) and green (with channeling). The regions allowed at 90% by a combination of the null experiments, excluding Super-Kamiokande, is indicated by the gray regions. Parameters in the overlapping regions (gray+orange or gray+green) are consistent with both the DAMA best fit regions and all null experiments. Super-Kamiokande constraints, if valid, would exclude all of the overlapping regions shown at 12 GeV (and all such regions with WIMP masses above 10 GeV).

in lighter shades of green and orange) are DAMA best fit parameters that satisfy the other constraints. Such regions can be found at masses of ~ 8 – 15 GeV. Above 10 GeV, these regions have $|a_p| \gg |a_n|$. At masses of 8–10 GeV, $|a_p| \gtrsim |a_n|$. SuperK constraints exclude all the overlapping regions above 10 GeV.

Figure 23 similarly shows constraints in the a_p - a_n plane, but shows the couplings compatible with the DAMA data within the 3σ level using a χ^2 g.o.f. test. Again, SuperK constraints are not included. Overlapping regions in this case are the parameters that are compatible with all experiments (within 3σ for DAMA and 90% for the others). Such regions are found over ~ 7 – 19 & 35 – 55 GeV without channeling and ~ 6 – 18 GeV with channeling. Inclusion of the SuperK constraint excludes all the overlapping regions above 10 GeV.

G. Mixed SI & SD Scattering

The SI only scattering case provides a slightly better fit to the DAMA modulation data than SD only scattering, as can be seen in Table IV, although the improvement is mild enough that each of the SI and SD spectra provide reasonable fits to DAMA. In the case of

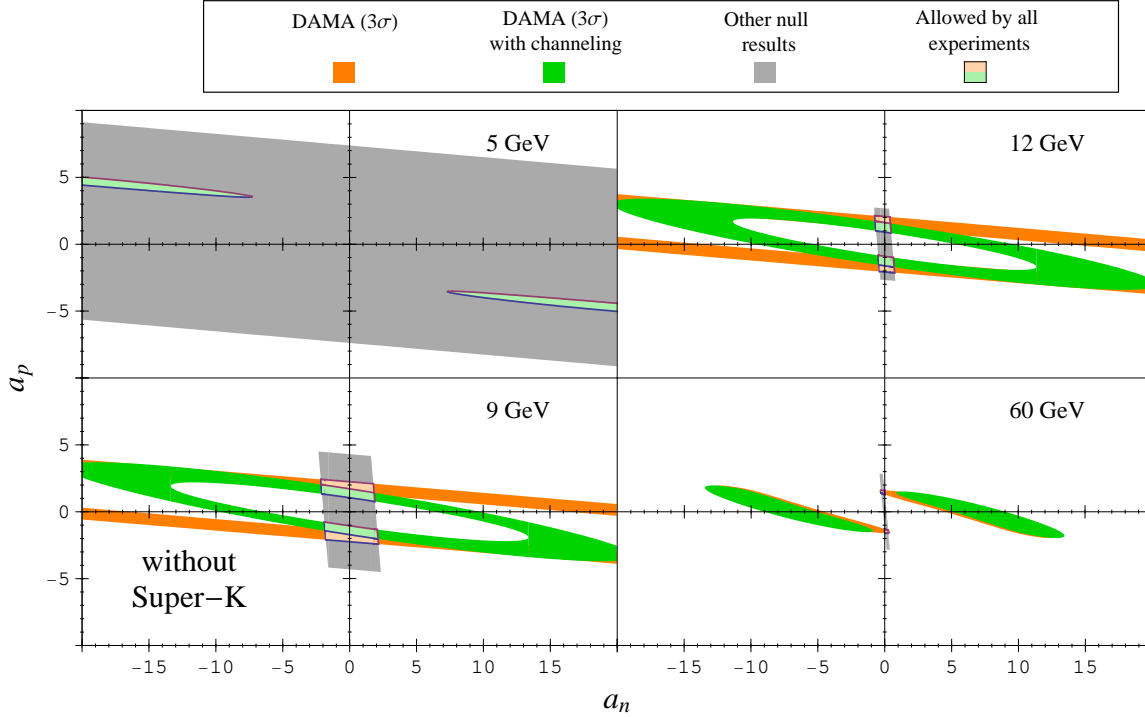


FIG. 23: Null experiment and DAMA constraints for SD only scattering in the a_p - a_n plane at several different WIMP masses. The 3σ allowed DAMA parameters are shown in orange (no channeling) and green (with channeling). The regions allowed at 90% by a combination of the null experiments, excluding Super-Kamiokande, is indicated by the gray regions. Parameters in the overlapping regions (gray+orange or gray+green) are consistent with all experiments. There is no DAMA region at 5 GeV without channeling that is compatible within the 3σ level. Super-Kamiokande constraints, if valid, would exclude all of the overlapping regions shown at 12 GeV and 60 GeV (and all such regions with WIMP masses above 10 GeV).

no channeling, SI only scattering actually provides the best global fit, but mixed SI and SD couplings can also provide reasonable fits (only slightly worse than the SI only case). With channeling, the best fit has a mix of SI and SD contributions.

Due to the linearity of the modulation amplitude and recoil events in each of the SI and SD cross-sections, $\sigma = \sigma_{\text{SI}} + \sigma_{\text{SD}}$, one may find approximate mixed SI and SD couplings by interpolating between the SI and SD only regions given in the various figures. For example, at a WIMP mass of 10 GeV, an SI-only WIMP-proton cross-section of 1.5×10^{-5} pb and an SD proton-only WIMP-proton cross-section of 1 pb each fall within the 90% g.o.f. constraints of their respective cases. Then the case where $\sim 60\%$ of the signal comes from SI scattering, with $\sigma_{\text{p,SI}} = 0.9 \times 10^{-5}$ pb (60% of the cross-section that gives the full signal in SI), and the other $\sim 40\%$ comes from SD scattering, with $\sigma_{\text{p,SD}} = 0.4$ pb (40% of the cross-section that gives the full signal in SD), should fall within (or very near) a 90% g.o.f. constraint in the mixed SI & SD coupling case. A variety of mixed SI & SD couplings for WIMP masses around ~ 8 GeV can be found that reasonably fit the DAMA data as well as the various null results of other experiments.

VI. CONCLUSIONS

The latest DAMA/LIBRA annual modulation data, which may be interpreted as a signal for the existence of weakly interacting dark matter (WIMPs) in our Galactic Halo, are examined in light of null results from other experiments. We investigate consequences for both spin-independent (SI) and spin-dependent (SD) WIMP couplings as well as mixed SI & SD couplings. The positive signal for annual modulation is compared to negative results from CDMS, CoGeNT, CRESST I, TEXONO, XENON10, and Super-Kamiokande (SuperK). In addition to the new experimental results, two new ingredients are included compared to our previous studies: 1) the energy spectrum of DAMA/LIBRA data is now given in 36 bins, and 2) the effect of channeling is taken into account, which lowers the nuclear recoil energy threshold and increases sensitivity to low WIMP masses. Several statistical tools are implemented in our study: best fit regions are found; goodness-of-fit (g.o.f.); and raster scans over the WIMP mass. These approaches allow us to differentiate between the most preferred (best fit) and allowed (g.o.f.) parameters. It is hard to find WIMP masses and couplings consistent with all existing data sets; the surviving regions of parameter space are found here. For SI interactions, the best fit DAMA regions of any WIMP mass are ruled out to 3σ , even with channeling taken into account. However, some parameters outside the best fit regions still yield a moderately reasonable fit to the DAMA data: we find parameters in the SI case at masses of $\sim 8\text{--}9$ GeV that are compatible with each of the experiments at better than the 3σ level when channeling is included. For SD interactions, we find no neutron-only couplings that are compatible with the DAMA data to within the 3σ level and satisfy other experimental constraints, with or without channeling included. For SD proton-only couplings, a range of masses below 10 GeV is compatible with DAMA and other experiments, with and without channeling, when SuperK indirect detection constraints are included; without the SuperK constraints, masses as high as ~ 20 GeV are compatible. Mixed couplings with $a_n = \pm a_p$ are found to be consistent with all experiments at ~ 8 GeV. The general case of mixed SD proton and neutron couplings are examined as well. In short, there are surviving regions at low mass for both SI and SD interactions (although only moderately so for the SI case) and at high masses for the case of SD proton-only couplings if indirect detection limits are relaxed.

While in the process of preparing this paper, several papers were presented that also examine the compatibility of the DAMA signal with other negative experimental results, always assuming that the dark matter consists of WIMPs [26, 67, 68, 69, 70, 71] (although other non-WIMP candidates were studied as well, such as mirror [72], composite [73], and WIMPlless [74] dark matter). Our results are compatible with the results of these other studies of WIMPs, although our conclusions sometimes differ. In all of them channeling is taken into account. Ref. [26] concludes that the recent CDMS results are compatible with the DAMA regions as derived by the DAMA collaboration, for WIMPs with spin independent interactions with mass in the 7 to 10 GeV range, a results similar to ours. Ref. [67] used only the raster scan and the DAMA data binned into two bins to study WIMPs with spin independent interactions (while here we use 36 data bins with this method) and find light WIMPs compatible with all experimental results, when channelling is included. Refs. [68] and [70] both studied WIMPs with spin independent interactions using global fits with two parameters and the data binned into many bins, thus including the spectral modulation amplitude information. Their results are similar to those of our global fits, but they conclude that light WIMPs with spin independent interactions “cannot account for the data” [68] or

“are strongly disfavoured” [70] within the standard halo model (they considered also the limits imposed by the DAMA total spectrum, not included here, which, however, affect heavier WIMPs). Ref. [71] studies indirect detection bounds which may be very important for light WIMPs, but depend on the WIMP-annihilation channels.

Acknowledgments

K.F. acknowledges the support of the DOE and the Michigan Center for Theoretical Physics via the University of Michigan. G.G. was supported in part by the US DOE grant DE-FG03-91ER40662 Task C. P.G. was partially supported by NSF grant PHY-0756962 at the University of Utah. C.S. acknowledges the support of the William I. Fine Theoretical Physics Institute at the University of Minnesota and thanks V. Mandic for useful conversations.

-
- [1] G. Jungman, M. Kamionkowski and K. Griest, Phys. Rept. **267**, 195 (1996) [arXiv:hep-ph/9506380].
 - [2] R. Bernabei *et al.*, Riv. Nuovo Cim. **26N1**, 1 (2003) [arXiv:astro-ph/0307403].
 - [3] R. Bernabei *et al.* [DAMA Collaboration], Eur. Phys. J. C **56**, 333 (2008) [arXiv:0804.2741 [astro-ph]].
 - [4] A. K. Drukier, K. Freese and D. N. Spergel, Phys. Rev. D **33**, 3495 (1986).
 - [5] K. Freese, J. A. Frieman and A. Gould, Phys. Rev. D **37**, 3388 (1988).
 - [6] D. S. Akerib *et al.* [CDMS Collaboration], Phys. Rev. D **68**, 082002 (2003) [arXiv:hep-ex/0306001].
 - [7] Z. Ahmed *et al.* [CDMS Collaboration], Phys. Rev. Lett. **102**, 011301 (2009) [arXiv:0802.3530 [astro-ph]].
 - [8] C. E. Aalseth *et al.*, Phys. Rev. Lett. **101**, 251301 (2008) [arXiv:0807.0879 [astro-ph]].
 - [9] J.I. Collar, private correspondence.
 - [10] E. Behnke *et al.* [COUPP Collaboration], Science **319**, 933 (2008) [arXiv:0804.2886 [astro-ph]].
 - [11] J.I. Collar and B. Odom, private correspondence.
 - [12] G. Angloher *et al.*, Astropart. Phys. **18**, 43 (2002).
 - [13] L. Stodolsky and F. Probst, talk at “The Dark Side of the Universe,” Ann Arbor, May 2004.
 - [14] H. S. Lee. *et al.* [KIMS Collaboration], Phys. Rev. Lett. **99**, 091301 (2007) [arXiv:0704.0423 [astro-ph]].
 - [15] S. T. Lin *et al.* [TEXONO Collaboration], arXiv:0712.1645 [hep-ex].
 - [16] H. T. Wong, private correspondence.
 - [17] J. Angle *et al.* [XENON Collaboration], Phys. Rev. Lett. **100**, 021303 (2008) [arXiv:0706.0039 [astro-ph]].
 - [18] J. Angle *et al.*, Phys. Rev. Lett. **101**, 091301 (2008) [arXiv:0805.2939 [astro-ph]].
 - [19] M. Brhlik and L. Roszkowski, Phys. Lett. B **464**, 303 (1999) [arXiv:hep-ph/9903468]; C. J. Copi and L. M. Krauss, Phys. Rev. D **67**, 103507 (2003) [arXiv:astro-ph/0208010]; R. Foot, Phys. Rev. D **69**, 036001 (2004) [arXiv:hep-ph/0308254]; R. Foot, Mod. Phys. Lett. A **19**, 1841 (2004) [arXiv:astro-ph/0405362]; A. M. Green, Phys. Rev. D **63**, 043005 (2001) [arXiv:astro-ph/0008318]; A. M. Green, Phys. Rev. D **66**, 083003 (2002)

- [arXiv:astro-ph/0207366]; G. Prezeau, A. Kurylov, M. Kamionkowski and P. Vogel, Phys. Rev. Lett. **91**, 231301 (2003) [arXiv:astro-ph/0309115]; P. Ullio, M. Kamionkowski and P. Vogel, JHEP **0107**, 044 (2001) [arXiv:hep-ph/0010036]; A. Kurylov and M. Kamionkowski, Phys. Rev. D **69**, 063503 (2004) [arXiv:hep-ph/0307185]; F. Giuliani and T. A. Girard, Phys. Rev. D **71**, 123503 (2005) [arXiv:hep-ph/0502232].
- [20] G. Gelmini and P. Gondolo, arXiv:hep-ph/0405278.
- [21] P. Gondolo and G. Gelmini, Phys. Rev. D **71**, 123520 (2005) [arXiv:hep-ph/0504010].
- [22] C. Savage, P. Gondolo and K. Freese, Phys. Rev. D **70**, 123513 (2004) [arXiv:astro-ph/0408346].
- [23] D. Tucker-Smith and N. Weiner, Phys. Rev. D **64**, 043502 (2001) [arXiv:hep-ph/0101138].
- [24] A. Gabutti, M. Olechowski, S. Cooper, S. Pokorski and L. Stodolsky, Astropart. Phys. **6**, 1 (1996) [arXiv:hep-ph/9602432].
- [25] A. Bottino, N. Fornengo and S. Scopel, Phys. Rev. D **67**, 063519 (2003) [arXiv:hep-ph/0212379].
- [26] A. Bottino, F. Donato, N. Fornengo and S. Scopel, Phys. Rev. D **78**, 083520 (2008) [arXiv:0806.4099 [hep-ph]].
- [27] J. Silk, K. A. Olive and M. Srednicki, Phys. Rev. Lett. **55**, 257 (1985); K. Freese and M. Kamionkowski, Phys. Rev. D **55**, 1771 (1997) [arXiv:hep-ph/9609370].
- [28] K. Freese, Phys. Lett. B **167**, 295 (1986); L. M. Krauss, M. Srednicki and F. Wilczek, Phys. Rev. D **33**, 2079 (1986).
- [29] S. Desai *et al.* [Super-Kamiokande Collaboration], Phys. Rev. D **70**, 083523 (2004) [Erratum-ibid. D **70**, 109901 (2004)] [arXiv:hep-ex/0404025].
- [30] J. Ahrens *et al.* [AMANDA Collaboration], Phys. Rev. D **66**, 032006 (2002) [arXiv:astro-ph/0202370].
- [31] M. Ackermann *et al.* [AMANDA Collaboration], Astropart. Phys. **24**, 459 (2006) [arXiv:astro-ph/0508518].
- [32] J. Ahrens *et al.* [The IceCube Collaboration], Nucl. Phys. Proc. Suppl. **118**, 388 (2003) [arXiv:astro-ph/0209556].
- [33] F. Blanc *et al.* [ANTARES Collaboration], *Presented by L. Thompson on behalf of the ANTARES Collaboration*, (ICRC 2003), Tsukuba, Japan, 31 Jul - 7 Aug 2003.
- [34] J. Silk and M. Srednicki, Phys. Rev. Lett. **53**, 624 (1984); J. R. Ellis, R. A. Flores, K. Freese, S. Ritz, D. Seckel and J. Silk, Phys. Lett. B **214**, 403 (1988); F. W. Stecker, S. Rudaz and T. F. Walsh, Phys. Rev. Lett. **55**, 2622 (1985).
- [35] P. Gondolo and J. Silk, Phys. Rev. Lett. **83**, 1719 (1999) [arXiv:astro-ph/9906391].
- [36] M. W. Goodman and E. Witten, Phys. Rev. D **31**, 3059 (1985).
- [37] P. F. Smith and J. D. Lewin, Phys. Rept. **187**, 203 (1990); J. D. Lewin and P. F. Smith, Astropart. Phys. **6**, 87 (1996).
- [38] J. Engel, Phys. Lett. B **264**, 114 (1991).
- [39] P. Gondolo, in *XXXI Rencontres de Moriond: Dark Matter in Cosmology, Quantum Measurements, Experimental Gravitation*, Les Arcs, France, 1996 [arXiv:hep-ph/9605290].
- [40] D. R. Tovey, R. J. Gaitskell, P. Gondolo, Y. Ramachers and L. Roszkowski, Phys. Lett. B **488**, 17 (2000) [arXiv:hep-ph/0005041].
- [41] P. Gondolo, J. Edsjo, P. Ullio, L. Bergstrom, M. Schelke and E. A. Baltz, JCAP **0407**, 008 (2004) [arXiv:astro-ph/0406204].
- [42] J. Engel, M. T. Ressell, I. S. Towner and W. E. Ormand, Phys. Rev. C **52**, 2216 (1995) [arXiv:hep-ph/9504322].

- [43] M. T. Ressell and D. J. Dean, Phys. Rev. C **56**, 535 (1997) [arXiv:hep-ph/9702290].
- [44] M. T. Ressell, M. B. Aufderheide, S. D. Bloom, K. Griest, G. J. Mathews and D. A. Resler, Phys. Rev. D **48**, 5519 (1993).
- [45] V. A. Bednyakov and F. Simkovic, Phys. Part. Nucl. **37**, S106 (2006) [arXiv:hep-ph/0608097].
- [46] B. Yanny *et al.*, Astrophys. J. **588**, 824 (2003) [Erratum-ibid. **605**, 575 (2004)] [arXiv:astro-ph/0301029].
- [47] H. J. Newberg *et al.*, Astrophys. J. **596**, L191 (2003) [arXiv:astro-ph/0309162].
- [48] S. R. Majewski, M. F. Skrutskie, M. D. Weinberg and J. C. Ostheimer, Astrophys. J. **599**, 1082 (2003) [arXiv:astro-ph/0304198].
- [49] K. Freese, P. Gondolo, H. J. Newberg and M. Lewis, Phys. Rev. Lett. **92**, 111301 (2004) [arXiv:astro-ph/0310334].
- [50] K. Freese, P. Gondolo and H. J. Newberg, Phys. Rev. D **71**, 043516 (2005) [arXiv:astro-ph/0309279].
- [51] A. M. Green, Phys. Rev. D **68**, 023004 (2003) [Erratum-ibid. D **69**, 109902 (2004)] [arXiv:astro-ph/0304446].
- [52] G. Gelmini and P. Gondolo, Phys. Rev. D **64**, 023504 (2001) [arXiv:hep-ph/0012315].
- [53] C. Savage, K. Freese and P. Gondolo, Phys. Rev. D **74**, 043531 (2006) [arXiv:astro-ph/0607121].
- [54] M. S. Armel-Funkhouser *et al.* [CDMS Collaboration], Phys. Rev. D **72**, 052009 (2005) [arXiv:astro-ph/0507190].
- [55] S. Yellin, Phys. Rev. D **66**, 032005 (2002) [arXiv:physics/0203002].
- [56] F. T. . Avignone, P. S. Barbeau and J. I. Collar, arXiv:0806.1341 [hep-ex].
- [57] P. Sorensen *et al.*, arXiv:0807.0459 [astro-ph].
- [58] L. Baudis, private correspondence.
- [59] A. M. Green, Phys. Rev. D **65**, 023520 (2002) [arXiv:astro-ph/0106555].
- [60] R. Bernabei *et al.* [DAMA Collaboration], Nucl. Instrum. Meth. A **592**, 297 (2008) [arXiv:0804.2738 [astro-ph]].
- [61] R. Bernabei *et al.*, Eur. Phys. J. C **53**, 205 (2008) [arXiv:0710.0288 [astro-ph]].
- [62] A. B. Migdal, J. Phys. USSR **4**, 449 (1941).
- [63] R. Bernabei *et al.*, Int. J. Mod. Phys. A **22**, 3155 (2007) [arXiv:0706.1421 [astro-ph]].
- [64] C. Amsler *et al.* [Particle Data Group], Phys. Lett. B **667** (2008) 1.
- [65] F. James, *Statistical methods in experimental physics*, Hackensack, NJ: World Scientific, (2006).
- [66] G. J. Feldman and R. D. Cousins, Phys. Rev. D **57**, 3873 (1998) [arXiv:physics/9711021].
- [67] F. Petriello and K. M. Zurek, JHEP **0809**, 047 (2008) [arXiv:0806.3989 [hep-ph]].
- [68] S. Chang, A. Pierce and N. Weiner, arXiv:0808.0196 [hep-ph].
- [69] S. Chang, G. D. Kribs, D. Tucker-Smith and N. Weiner, arXiv:0807.2250 [hep-ph].
- [70] M. Fairbairn and T. Schwetz, arXiv:0808.0704 [hep-ph].
- [71] D. Hooper, F. Petriello, K. M. Zurek and M. Kamionkowski, arXiv:0808.2464 [hep-ph].
- [72] R. Foot, Phys. Rev. D **78**, 043529 (2008) [arXiv:0804.4518 [hep-ph]].
- [73] M. Y. Khlopov and C. Kouvaris, Phys. Rev. D **78**, 065040 (2008) [arXiv:0806.1191 [astro-ph]]; M. Y. Khlopov, arXiv:0806.3581 [astro-ph]; C. Kouvaris, Phys. Rev. D **78**, 075024 (2008) [arXiv:0807.3124 [hep-ph]].
- [74] J. L. Feng, J. Kumar and L. E. Strigari, Phys. Lett. B **670**, 37 (2008) [arXiv:0806.3746 [hep-ph]].